Interactions and triggering in a 3-D rate-and-state asperity model

Pierre Dublanchet, Pascal Bernard, P. Favreau

▶ To cite this version:

Pierre Dublanchet, Pascal Bernard, P. Favreau. Interactions and triggering in a 3-D rate-and-state asperity model. Journal of Geophysical Research : Solid Earth, 2013, 118 (5), pp.2225 - 2245. 10.1002/jgrb.50187 . hal-01386351

JOURNAL OF GEOPHYSICAL RESEARCH: SOLID EARTH, VOL. 118, 2225–2245, doi:10.1002/jgrb.50187, 2013

Interactions and triggering in a 3-D rate-and-state asperity model

P. Dublanchet,[1] P. Bernard,[1] and P. Favreau[1]

Received 30 September 2012; revised 2 April 2013; accepted 9 April 2013; published 17 May 2013.

[1] We present a 3-D continuous quasi-dynamic rate-and-state model of multiple seismic asperities forced by surrounding aseismic creep and motivated by observations of coplanar multiplets. Our model allows to study the physics of interactions among a set of asperities. First, we show that the amount of interactions and clustering, characterized by the Omori law and interevent time distribution, depends on how far the system is from a critical density of asperities, which is related to the friction properties of the barriers separating the sources. This threshold controls the ability of a population of asperities to destabilize the creeping barriers between them and therefore determines whether dynamic sequences including several asperities in the same event might occur, in agreement with what is expected from observed magnitude-frequency distributions. Therefore, the concept of critical density of asperity provides a mechanical interpretation of statistical properties of seismicity. As an illustration, we used our numerical results in the specific case of Parkfield in the period preceding the M_W6, 2004 earthquake, in order to infer the steady state friction parameter $(a-b)$ characterizing the creep of this part of the San Andreas Fault. We estimate a value of $(a-b)$ that locally exceeds 0.001, which is in the upper range of what has already been proposed for the postseimic period of the M_W6, 2004 Parkfield earthquake.

Citation: Dublanchet, P., P. Bernard, and P. Favreau (2013), Interactions and triggering in a 3-D rate-and-state asperity model, *J. Geophys. Res. Solid Earth*, *118*, 2225–2245, doi:10.1002/jgrb.50187.

1. Introduction

[2] Recent advances on the understanding of microseismicity include the observation of repeating earthquakes that have been reported on several faults in the world such as the Parkfield segment of San Andreas fault in California [*Nadeau et al.*, 1995; *Nadeau and McEvilly*, 1997; *Nadeau and Johnson*, 1998; *Nadeau and McEvilly*, 1999; *Lengliné et al.*, 2009], the Hayward fault in northern California [*Bürgmann et al.*, 2000], the north-eastern Japan subduction zone [*Matsuzawa et al.*, 2002; *Igarashi et al.*, 2003], and the North Anatolian fault in Turkey [*Peng and Ben-Zion*, 2005; *Bouchon et al.*, 2011]. These events are small regular ruptures that occur on a single fault patch (asperity), generating similar waveforms at recording stations. The occurrence of several events on the same asperity is a strong indicator that these seismic sources are forced by surrounding aseismic slip on the faults [*Nadeau et al.*, 1995; *Igarashi et al.*, 2003; *Bürgmann et al.*, 2000], and consequently, the recurrence time of such repeaters has been widely used to infer local aseismic slip rates on faults [*Nadeau and McEvilly*, 1999; *Bürgmann et al.*, 2000; *Igarashi et al.*, 2003].

[3] In addition to the coupling between seismic and aseismic sliding, another characteristic of microseismicity is the existence of a wide range of temporal behaviors, including seismic swarms, mainshock-aftershock sequences that suggest the importance of triggering and interaction phenomena among seismic sources. Moreover, the complex behavior of microseismicity contrasts with the existence of regular repeating earthquakes, and to interpret this contradiction we have to consider, in addition to isolated asperities, systems of interacting sources. Despite this apparent complexity, robust empirical laws emerge from the observation of seismicity: the Omori law characterizing the decay of aftershock rate [*Utsu et al.*, 1995] and the Gutenberg-Richter law [*Gutenberg and Richter*, 1956] corresponding to the magnitude-frequency distribution of earthquakes. Associated with the Omori decay, *Utsu et al.* [1995] and *Hainzl et al.* [2006] analyzed simple statistical laws describing the distribution of time delays between successive events. According to these authors, this kind of statistics is an indicator of the amount of interaction among a population of seismic sources. In addition to the bare Omori law characterizing the decay of direct aftershocks, *Helmstetter and Sornette* [2002] and *Marsan and Lengline* [2008] studied the so called "dressed" or "renormalized" Omori law that takes into account all the possible aftershocks of aftershocks which is a way to better constrain the processes of multiple triggering in aftershock sequences.

[4] Based on the empirical laws, several attempts have been made to produce realistic synthetic catalogs such as Epidemic-Type Aftershock Sequence (ETAS) models

---

[1] Laboratoire de Sismologie, Institut de Physique du Globe de Paris, Paris, France.

Corresponding author: P. Dublanchet, Institut de Physique du Globe de Paris, 1, rue Jussieu - 75238 Paris CEDEX 05, France. (dublanchet@ipgp.fr)

2169-9313/13/10.1002/jgrb.50187

introduced by *Ogata* [1988], *Kagan and Knopoff* [1981], and *Kagan and Knopoff* [1987]. These models all share a common hypothesis of linearity, because each event triggers its own aftershock sequence, and the resulting seismicity is the sum of all these effects. On the other hand, rock friction experiments conducted by *Dieterich* [1979] show a highly nonlinear behavior of rocks during earthquake processes, suggesting that triggering during aftershock sequences is affected by nonlinear friction. Therefore, the global triggering effect might be modulated by nonlinear response of seismic sources, and the response of several stress perturbations might be somewhat different than the sum of all mainshock-aftershocks sequences as this is assumed in ETAS models. Furthermore, nonlinear rate-and-state friction [*Dieterich*, 1979; *Rice and Ruina*, 1983; *Ruina*, 1983] has been successful in explaining many other aspects of seismic behavior, including earthquake nucleation [*Dieterich*, 1992] or aftershock decay [*Dieterich*, 1994], therefore appearing as an important aspect of earthquake physics.

[5] Motivated by friction experimental results, more mechanical models have nevertheless been proposed to produce a realistic seismicity. That is, for instance, the case of discrete models of faults that include rate-and-state friction as well as realistic stress interaction kernels [*Dieterich*, 1995; *Ziv and Rubin*, 2003; *Ziv and Cochard*, 2006]. Although these models are able to produce satisfying statistics, including Omori decay and Gutenberg-Richter distribution, they are limited by the impossibility to obtain realistic nucleation because of over-sized computational cells compared to the critical length for nucleation predicted by rate-and-state theory [*Rice and Ruina*, 1983; *Ruina*, 1983], or to group computational cells in order to define asperities since all the cells are independent.

[6] In the present study, we propose a continuous, 3-D rate-and-state model of fault that allows to define multiple asperities embedded in a planar creeping fault, in order to fully describe what might be realistic sources of microseismicity, more specifically for sets of multiplets and repeaters. Such multiple asperity models associating aseismic sliding and earthquakes have already provided some important insights in the processes of interaction between seismic sources, especially concerning the migration of aftershocks as shown by *Kato* [2007], but also in the understanding of low-frequency earthquakes behavior in subduction zones [*Ariyoshi et al.*, 2012]. In this study, we focused on the background seismic activity and attempted to generate synthetic catalogs of events characterized by realistic statistical properties, and we illustrate it in the specific case of the Parkfield seismicity, as was relocated by *Lengliné et al.* [2009].

[7] In the following, we first introduce and illustrate the various statistics (generalized Omori law, interevent time distribution, and magnitude frequency distribution) on the Parkfield observations and briefly comment on their features. We then present our rate-and-state asperity model, recalling the basic equations and describing the specific model parameters relevant for our study (geometry, friction, initial, and boundary conditions). This allows us to address the question of the influence of barriers and distribution of asperities on the event statistics. In a first part, we analyze the results obtained for a simple distribution of asperities that outlines the concepts that are relevant in interaction processes among a population of asperities. Then, we show how these concepts could be formalized using a critical density of asperities theory. Finally, we briefly revisit and discuss the observational results of Parkfield.

2. Parkfield Seismicity

[8] We analyzed the event statistics of Parkfield provided by *Lengliné et al.* [2009]. This catalog spans more than 20 years between 1984 and 2007. During this period of time, one magnitude 6.0 occurred on the 28th of September 2004. *Lengliné et al.* [2009] relocated precisely more than 8000 events occurring in this area and recorded by the Northern California Seismic Network, by relative relocation after the identification of multiplets. These multiplets allowed precise relative timing through cross-correlation, allowing accurate double difference relocation. The criteria used to define multiplets were a mean coherency of 90%, a source overlap greater than 70%, and a magnitude difference between two events lower than 0.2. The results of relocation are shown in Figure 1.

[9] In order to estimate the size of each seismic rupture, we followed the procedure used by the authors, based on the moment M_{0e} of the events. The seismic moment for a circular crack of radius R with constant stress drop $\Delta\tau_a$ is given by the following:

$$M_{0e} = \frac{16}{7}\Delta\tau_a R^3. \tag{1}$$

[10] We present in Figure 1 an example of computed source sizes using a stress drop of 3 MPa (in the range of what is inferred at Parkfield by *Dreger et al.* [2007]), as well as the evolution of the same sequence in a space-time plot. This precise relocation and first-order evaluation of seismic size illustrates the fact that microseismicity occurs on small patches of the fault, with several events occurring at the same place (repeaters) surrounded by areas without any events and often interpreted as being aseismic. The example detailed in Figure 1 nevertheless highlights the fact that repeaters are not necessarily isolated on the fault but instead form clusters of overlapping asperities. Furthermore, the occurrence of events on this composite structure is far from being regular in time (Figure 1c). This type of multiplet cluster will be the basis of our modeling.

[11] In addition to these observations, we computed three kinds of statistics with the catalog. The first one is the interevent time distribution defined by *Hainzl et al.* [2006] as follows: we plotted in Figure 2 the corresponding density function in different cases. First, for the whole area, considering successively: events before the M_w6 mainshock, events after it, and all the events of the catalog. Furthermore, we considered that distribution of delays smaller than 100 s were irrelevant, because of biased detection associated with the coda waves. Since the inter-event time distribution is strongly affected by the M_w6 earthquake of 2004, we focused on the events occurring before 2004, and we ended up with a distribution that at short time could be characterized by a power law of the form $\tilde{dt}^{-p^*}$ with a p^* of 0.54, $\tilde{dt}$ being the inter-event time dt normalized by the mean value of the inter-event time delays of the entire sequence ($< dt >$), so that $\tilde{dt} = dt/ < dt >$. Then, we proceeded in the same way to evaluate this distribution at different places on the fault where sufficient events occurred prior to 2004 (more than

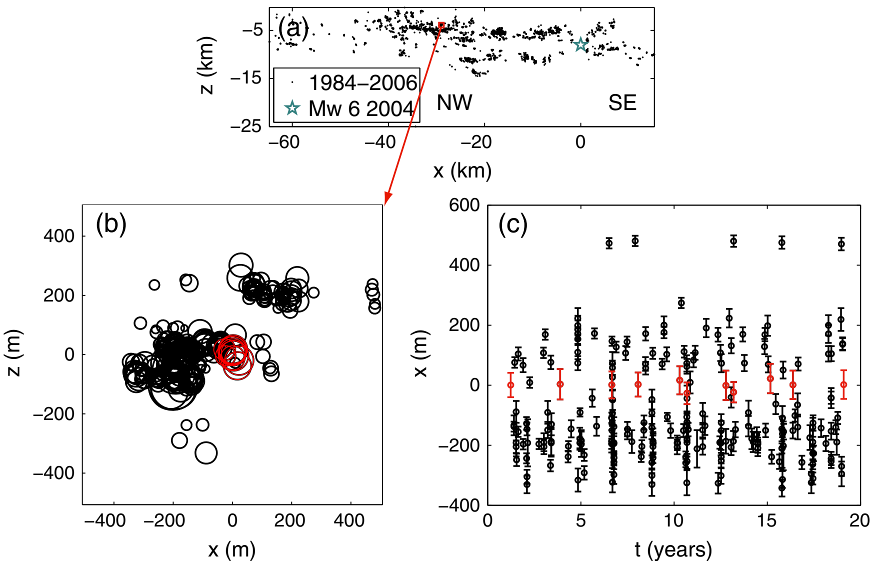

Figure 1. (a) Location of 22 years of seismicity (black dots) between 1984 and 2006 on Parkfield segment of the San Andreas fault from *Lengliné et al.* [2009]. x is the distance along strike, and z is the depth. Blue star is the hypocenter of the M_w6 earthquake of September 2004. The red rectangle locates the inset of Figure 1b. (b) Zoom on the fault, showing events occurring before the M_w6 event, x, and z are the same as in Figure 1a. Each circle represents the approximate size of each event deduced from its magnitude, assuming a constant stress drop of 3 MPa. Red circles correspond to a particular multiplet. (c) Location along strike versus time for the events of Figure 1b. Time zero corresponds to the first of January 1984. Red dots are for the events belonging to the same multiplet as in Figure 1b, and error bars indicate the extent of each rupture.

100 events in a box), and we obtained values of p^* ranging from 0.56 to 0.9, with a mean value of 0.76.

[12] As another characterization of the seismic activity of Parkfield, we computed the generalized Omori law. We considered successively all the events of the catalog as mainshocks, and we stacked all the sequences that we obtained for these different main events. Furthermore, we excluded all the earthquakes occurring after 2004 to focus on the properties of the background activity. The global and local results are presented in Figure 2, giving short time slopes between 100 s and 1 day ranging from $p = 0.53$ to 0.83, with a mean value of $p = 0.65$, corresponding to an averaged seismicity rate decaying as t^{-p}, t being the time following the mainshock.

[13] Finally, we computed the magnitude-frequency distribution for all the events relocated at a global and a local scale. In order to enhance the variability in slopes, we normalized the distribution by its maximum, and we plotted the results in Figure 2. The slope b^* (referred as $-b$ parameter of the Gutenberg-Richter law) that characterizes the magnitude-frequency distribution ranges between $b^* = 0.86$ and $b^* = 1.79$, with a mean value of $b^* = 1.23$.

[14] More generally, *Utsu et al.* [1995] indicates that real mainshock-aftershocks sequences, which represent the same process of interaction than what is leading to the composite decay we are calculating, are characterized by values of p between 0.9 and 1.5. The generalized Omori decay obtained here could also be compared with the dressed kernels computed by *Marsan and Lengline* [2008] for the seismicity of California, resulting in p values ranging between 0.6 and 1.0 which is less than what is observed for direct aftershocks. Furthermore, classical values for magnitude-frequency distributions are mostly between 0.5 and 1.5 [*Utsu*, 1972]. Finally, the value of $p^* = 0.54$ indicates according to *Hainzl et al.* [2006] and *Molchan* [2005] a level of Poissonian background activity of 46%, and the clear difference between the values of p^* before and after the mainshock, increasing from 0.54 to 0.81, shows a larger amount of correlated seismicity after the main event, as expected for an aftershock sequence.

[15] In the following, we will focus on the asperity model which could be relevant for Parkfield and, more generally, for similar multiplet-prone areas, before discussing the Parkfield case further on.

3. Model of Asperities

3.1. Rate-and-State Friction

[16] In the following, we consider a 2-D fault plane embedded in a 3-D, homogeneous elastic space as shown in Figure 3, and we divide it in 256 by 256 cells. Motion is forced at a constant rate v_p in the x direction imposed at a distance w above the fault plane, and sliding is resisted by rate-and-state friction [*Dieterich*, 1979; *Rice and Ruina*, 1983] expressed as follows:

$$\tau_{xz,i} = \sigma \left[\mu_0 + a_i \ln \frac{v_i}{v_p} + b_i \Theta_i \right], \qquad (2)$$

where $\tau_{xz,i}$, v_i, and Θ_i refer respectively to the frictional shear stress, the velocity, and the state variable on the cell i. For a matter of simplicity, we will replace $\tau_{xz,i}$ by τ_i in the rest of the manuscript. The state variable is thought to be an indicator of microscopic contact strength [*Dieterich*, 1979; *Ruina*, 1983], which might evolve with time and slip

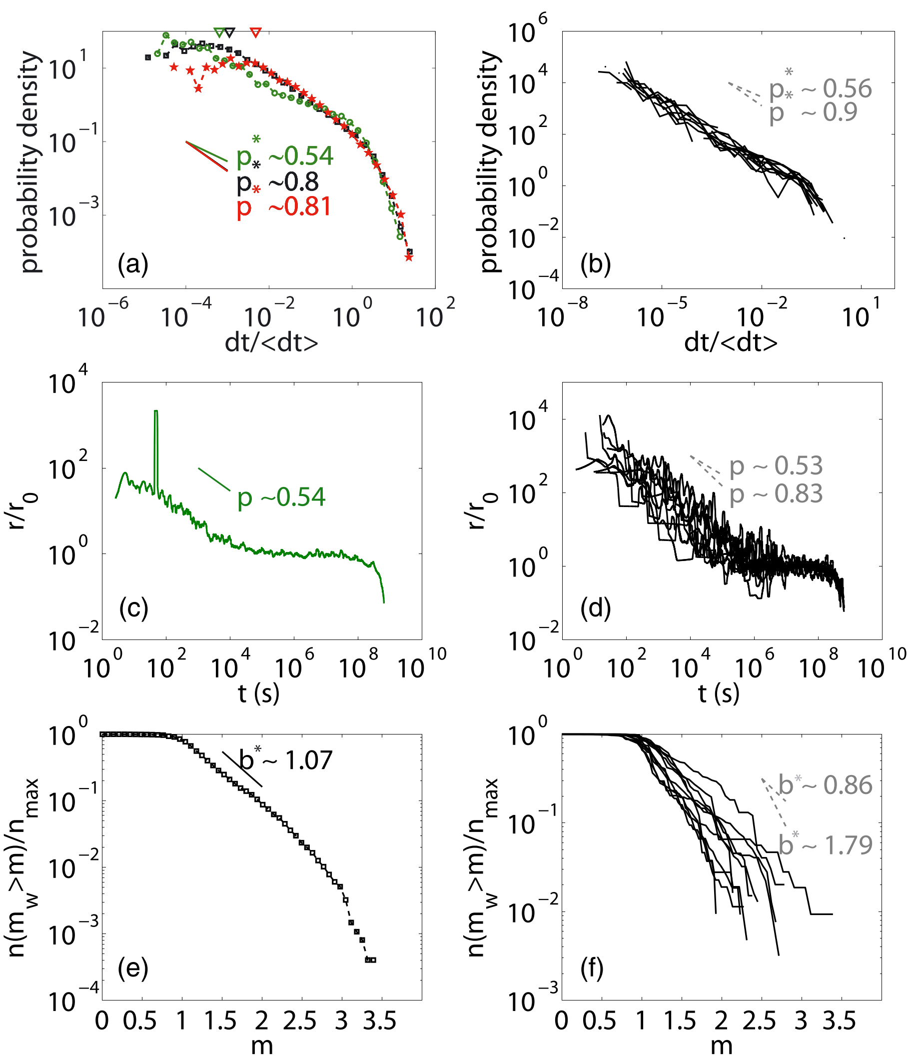

Figure 2. (a) Normalized inter-event time distribution for events that occurred before the M_w6 (green dots), after the M_w6 (red stars), and for the whole time period (black squares). $< dt >$ is the mean interevent time, and dt is the interevent time. The triangles correspond to 100 s. The slope obtained for a fit between 100 s and $dt/ < dt >= 10^{-1}$ is represented each time by the straight line. (b) Same as Figure 2a but each curve corresponds to different areas of the fault. We selected the events before M_w6. (c) Generalized Omori law for the events before M_w6. t is the time since each mainshock, r is the seismicity rate, and r_0 is the background seismicity rate. The fit of the curve between 100 s and 1 day is shown with the green straight line. (d) Same as Figure 2c but at a smaller scale for the different parts of the fault. (e) Magnitude-frequency distribution for all the events recorded. m and m_w are the moment magnitudes, n is the number of earthquakes, and $n_{\max}$ is the maximum number of events. The black straight line is the fit of the distribution for magnitudes greater than 1.2. (f) Same diagram as Figure 2e but for the different areas of the fault.

history of the interface. σ is the normal stress that is considered constant, μ_0 is the friction coefficient when the system experiences steady sliding at a velocity equal to v_p, and a_i and b_i are nondimensional constitutive parameters. As shown by *Dieterich* [1979], equation (2) reflects the fact that frictional strength increases with true microscopic contact area which fluctuates with v and Θ. Furthermore, we need to specify a time evolution law for the state variable Θ: Here, we chose to work with the aging evolution law described by *Ruina* [1983] as follows:

$$\dot{\Theta}_i = \frac{v_p}{d_c} e^{-\Theta_i} - \frac{v_i}{d_c}, \qquad (3)$$

where d_c is the characteristic slip necessary to renew a population of microscopic contacts.

[17] At steady state, the right-hand term in equation (3) vanishes, and the frictional strength of equation (2) takes the following form:

$$\tau_i^{ss} = \sigma \left[\mu_0 + (a_i - b_i) \ln \frac{v_i}{v_p} \right], \qquad (4)$$

showing that if sliding velocity is constant, then the friction coefficient evolves toward a constant value after a characteristic displacement that scales with d_c. The new friction coefficient depends on a and b parameters, exhibiting two

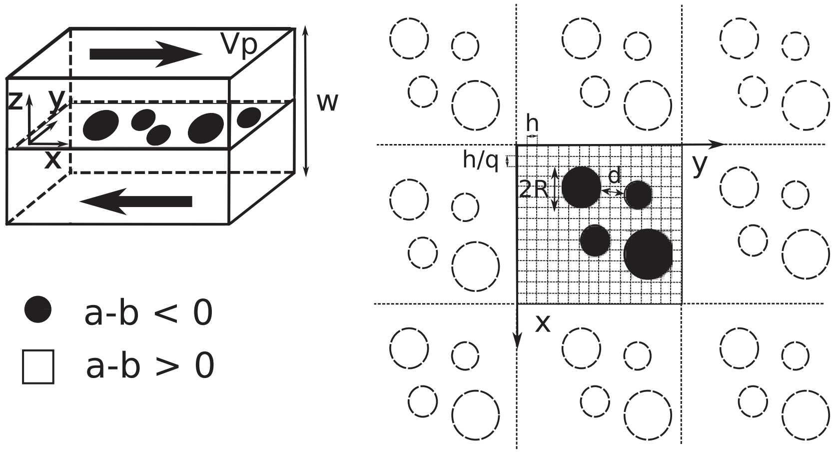

Figure 3. (left) Schematic diagram showing the fault with velocity weakening asperities ($a - b < 0$), creeping areas ($a - b > 0$), and loading direction. w is the distance at which loading rate is controlled. (right) View of the fault plane, with asperities of radius R separated by d, and computational cells of size h/q by h. Dashed asperities correspond to the images of the fault plane in the x and y directions.

kinds of behavior: either velocity strengthening for positive $a - b$, or velocity weakening for negative $a - b$. Linear stability analysis of the rate-and-state spring and slider motion around steady state conducted by *Rice and Ruina* [1983] and *Ruina* [1983] shows that steady sliding is always stable as long as $a-b$ is positive but conditionally stable when velocity weakening properties govern the system. In the latter case, the critical maximum stiffness k_c needed to obtain frictional instability is given by the following:

$$k_c = \frac{(b-a)\sigma}{d_c}. \tag{5}$$

In order to model asperities on the fault plane, we will follow [*Kato*, 2003] and define patches that are potentially unstable, that is with velocity weakening friction properties, and surrounded by creeping areas experiencing velocity strengthening steady state friction as shown in Figure 3. Since in our 3-D continuous model, the stiffness of an asperity is related to its size, we specify that the velocity weakening areas are over-sized with respect to a critical size. In order to have a rough estimate of this critical size, we use the developments of *Rubin and Ampuero* [2005] about nucleation on 2-D velocity weakening faults governed by the aging state evolution law. *Rubin and Ampuero* [2005] showed that depending on a/b parameter, the region of high slip rate either approximately localizes over a length scale noted L_b ($0 < a/b < 0.3781$) or expands as a quasi-static crack ($0.3781 < a/b < 1$), and in this latter case, seismic instability is reached when high slip speeds affect a region of half-width noted R_c. L_b and R_c depend on the friction parameters a and b of the weakening fault and are given by the following:

$$L_b = \frac{\mu d_c}{b\sigma}, \tag{6}$$

$$R_c = \frac{\mu b d_c}{\pi\sigma(b-a)^2}, \tag{7}$$

where μ is the shear modulus of the elastic space. Furthermore, according to *Chen and Lapusta* [2009] who present the result of (A. Rubin, private communication, 2008) the length R_c in a 3-D situation should be larger by a factor of $\pi^2/4$ than what is expected from equation (7). In the following, we used the largest value of L_b or R_c as the minimum radius for asperities.

[18] Another important requirement is to build a continuous fault model, in the sense given by [*Rice*, 1993] that all the cells of the computational grid have to be smaller than the critical size for instability. This property ensures that all the cells within an asperity will break in the same event, preventing independent ruptures inside the structure. In this sense, we build a different model from the one used by *Dieterich* [1995], *Ziv and Rubin* [2003], and *Ziv and Cochard* [2006]. In addition to this, we require the model to generate a realistic earthquake cycle on asperity, in particular during nucleation. To ensure a correct description of nucleation *Dieterich* [1992], *Rubin and Ampuero* [2005], and *Ampuero and Rubin* [2008] showed that the cell size should be smaller than L_b given by equation (6).

[19] In the next parts, we will call anti-asperity or barriers, or creeping barriers, the creeping areas surrounding the asperities and experiencing velocity strengthening friction. We will refer to friction on the weakening asperities as a_w, b_w, and $(b - a)_w$, and for the friction on the anti-asperity as a_s, b_s, and $(a - b)_s$, respectively.

3.2. Quasi-dynamic Stress Interactions

[20] We model quasi-dynamic elastic interactions between the different parts of the fault with the elastic kernel used by *Kato* [2003] and formalized by *Maruyama* [1964] on the one hand, and the radiation damping term first introduced by *Rice* [1993] on the other hand. Consequently, the elastic shear stress τ_i on the cell i of the fault is expressed as follows:

$$\tau_i = \tau^* - \frac{\mu}{w}(\delta_i - v_p t) + \sum_j k_{ij}(\delta_j - v_p t) - \eta(v_i - v_p), \tag{8}$$

where τ^* is a constant, μ is the shear modulus, δ_j is the displacement of cell j in the x direction, and k_{ij} is the shear stress generated at a point i due to the displacement on a rectangular dislocation centered at a point j on the fault, from the solution of *Maruyama* [1964].

[21] The second term on the right-hand side of equation (8) corresponds to the constant loading contribution to stress, introduced by *Dieterich* [1995], and further implemented by *Ziv and Rubin* [2003] and *Ziv and Cochard* [2006]. This latter term accounts for the stressing associated with the motion at constant rate v_p at a distance $w/2$ above the fault plane, as this is depicted in Figure 3.

[22] The third term on the right-hand side of equation (8) is the result of elastostatic interactions between each dislocation in the fault plane. According to *Maruyama* [1964], the elastic kernel k_{ij} is computed using a Green function characterizing a semi-infinite elastic half space that is not compatible with our block geometry, where motion is prescribed at a distance $w/2$ of the fault. Therefore, this conceptual approximation might introduce some error in the long range stress interactions. However, we show in Appendix A that owing to the small ratio between the fault length and the block width $w/2$, this error is negligible.

[23] We further add in this expression the radiation effect, where η is the damping introduced by *Rice* [1993]: This term is an approximation of the elastodynamic effects in the sense that it corresponds to the stress drop associated with the emission of shear waves in the fault normal direction. Introducing the radiation damping prevents the slip velocity from becoming unbounded on the fault and allows for the computation of multiple seismic cycles. The damping is a function of shear wave velocity c_s and shear modulus μ, given by:

$$\eta = \frac{\mu}{2c_s}. \tag{9}$$

Finally, in order to allow the use of efficient fast Fourier transform (FFT) techniques as will be detailed later, we consider a periodic repetition of the fault plane in the x and y directions as shown in Figure 3, so that k_{ij} represents the stress on a point i due to simultaneous slip on a point j and on every images of j.

3.3. Computation Method

[24] Assuming equality between frictional stress (2) and quasi-dynamic elastic stress (8) and differentiating with respect to time, we obtain the following equation for $\dot{v}_i$ after substituting the aging evolution law (3) for $\dot{\Theta}$ as follows:

$$\dot{v}_i = \frac{v_i}{\eta v_i + a_i\sigma}\left[-\frac{\mu}{w}(v_i - v_p) + \sum_j k_{ij}(v_j - v_p) + \frac{b_i\sigma}{d_c}\left(v_i - v_p e^{-\Theta_i}\right)\right]. \tag{10}$$

From this last point, equation (10) together with the aging evolution law (3) for Θ constitute a set of first-order differential equations, that is solved using a fourth-order adaptative time step Runge-Kutta algorithm [*Press et al.*, 2007]. In order to reduce the number of free parameters, we normalized all the quantities, as shown in Appendix B. The time step adaptation method is based on the estimation of the maximum amplitude eigenvalue of the linearized system associated with the problem. More details about this computation are provided in Appendix C. The most time consuming part of the computation is the evaluation of the elastostatic interactions which involves a convolution in space, but since the velocity and stress fields are periodic in horizontal directions, we use efficient 2-D FFT routines developed by *Swarztrauber* [1982] and *Swarztrauber* [1984] to compute these elastic stressing.

[25] Furthermore, we parallelized the computation of the Runge-Kutta algorithm using MPI library [*Pacheco*, 1997].

3.4. Model Parameters

[26] In the next sections, we used square computational cells with $h = 3$ m and $q = 1$ (Figure 3), and following *Rice* [1993], we assumed a constant normal stress of 100 MPa, that could be the effective pressure expected at about 5 km depth in a fault affected by elevated pore pressure, as proposed by *Rice* [1992]. We did not consider a depth variable normal stress since the fault plane we focus on is about one by one kilometer large, which would correspond to a change in lithostatic normal stress of 10 to 30 percent, that would in addition be balanced by a pore pressure increase of the same amount [*Rice*, 1992]. Furthermore, we assumed a loading rate of 10^{-9} m s^{-1} (i.e., 3.15 cm yr^{-1}) which is in the range of the creep rate measured on the Parkfield segment (2.5 cm yr^{-1}) as shown by *Harris and Segall* [1987], *Murray et al.* [2001], and *Titus et al.* [2006]. Concerning friction parameters, we followed *Marone* [1998] so that we made our simulations with $\mu_0 = 0.6$, $0.006 > (a - b)_{w,s} > -0.006$ and $d_c = 0.2$ mm. The Lame parameters λ and μ were assumed constant and equal to 30 GPa in the elastic medium, and the damping was taken constant at 5 MPa s m^{-1} which is the value expected from equation (9) for a shear wave velocity of 3 km s^{-1}. We also chose $w = 3$ km for the elastic loading, which is about 3 times the fault length. Thus, w was large enough so that it did not directly influence slip rate on the fault plane, and small enough to allow fast convergence of the slip rate to the stationary state of the system after initialization.

[27] Following *Kato* [2003, 2004, 2007], and *Chen and Lapusta* [2009], we defined circular asperities on the fault plane assuming a radius of asperity in the range of what could be the size of seismic sources in Parkfield, that is around 30 m (Figure 1). Furthermore, the friction parameters on the asperities were assumed constant in our simulations: We chose $a_w = 0.001$ and $b_w = 0.005$, leading to a value of $(b - a)_w$ that prevents unrealistic stress drop during a seismic event, since this drop scales with $(b - a)_w$ as shown by *Tse and Rice* [1986]. With these asperity parameters, we obtained stress drops of the order of 6 MPa. This value is in agreement with the estimations at Parkfield, ranging from around 2 MPa [*Dreger et al.*, 2007] to 200 MPa [*Nadeau and Johnson*, 1998]. Moreover, this choice resulted in asperities with a radius R of about $1.02R_c$ ($R_c \sim 29.4$ m), a $L_b \sim 12$ m on the asperity and as we used square cells of size h by h with $h = 3$ m, this led to a ratio h/L_b of 0.25 which usually allows a rather correct nucleation on the asperities.

3.5. Initial Conditions and Global Steady State

[28] For initial conditions, we had to prescribe values of v and Θ through all the fault plane. We did our choice in a somewhat arbitrary way by imposing a steady state ($\Theta = 0$) at $v = v_p$ on all the velocity strengthening areas of the fault so that the creep initially followed the loading. On the other hand, we imposed that the population of asperities had to be initially uniformly distributed in their own seismic cycle, in order to prevent an eventual synchronization of the sources. For that, we chose an initial $\Theta = 3.2$ and a uniform distribution of velocity between $10^{-26}v_p$ and v_p. These conditions indeed sample

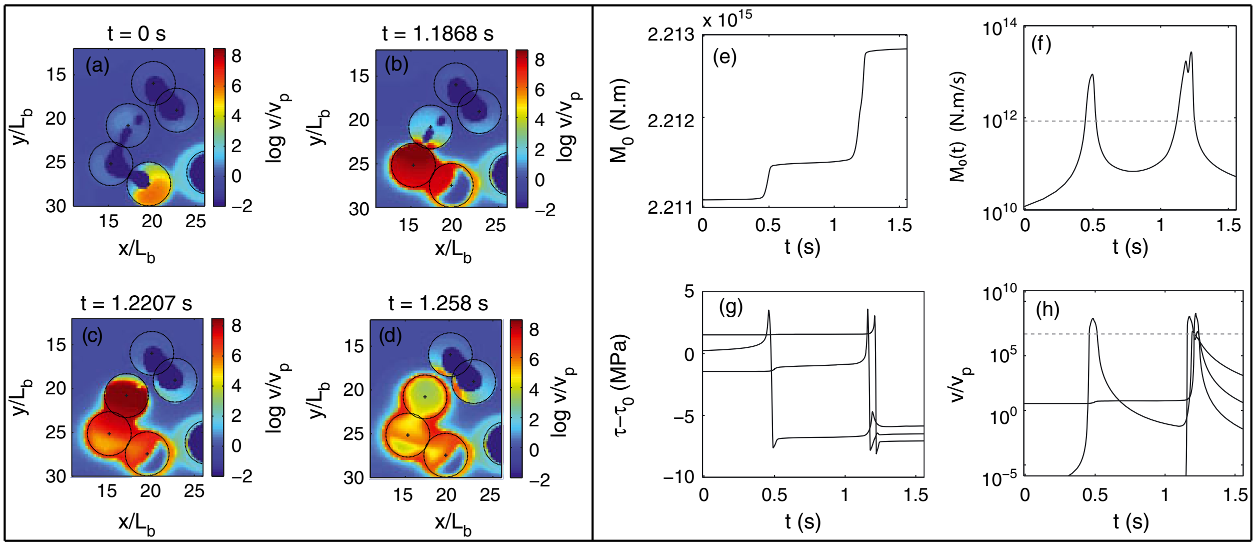

Figure 4. The four left panels (a–d) represent snapshots of the logarithm of normalized sliding velocity. v is the velocity, v_p is the loading rate, x is the direction of loading, and y is the orthogonal direction. Each panel zooms on the same group of asperities, defined by the black circles. Black crosses represent the centers of the asperities. The four right panels represent the evolution with time of (e) cumulative moment released on the fault plane M_0, (f) moment release rate $\dot{M}_0$, (g) shear stress $\tau - \tau_0$ at the center of each asperity represented on the left panels, and (d) normalized sliding velocity v/v_p at the center of the asperities. On the moment rate and velocity curves, the gray dashed line represents respectively the threshold of moment rate $\dot{M}_{0s}$ defined by equation (12) above which radiation of waves occurs, and the velocity v_{sis} = 1 cm s^{-1}. Friction parameters on the asperity are a_w = 0.001, b_w = 0.005, while the anti-asperity is characterized by a_s = 0.007 and b_s = 0.005. Other parameters are defined in the text.

quite well the interseismic part of the seismic cycle but are rather unrealistic in the sense that the calculation starts with very large velocity and stress gradients at the transition between asperities and creeping segment. Therefore, the system progressively relaxes to its own global cycle which starts when the mean cumulative displacement follows the loading displacement.

3.6. Building Synthetic Catalog

[29] At the end of one simulation, we obtain the evolution through time of slip velocity, state, and shear stress on each point of the fault plane, as well as the cumulative moment released $M_0(t)$ by this structure. The latter quantity is calculated using the following expression:

$$M_0(t) = \mu \sum_i \frac{h^2}{q} \delta_i(t), \tag{11}$$

where μ is the shear modulus, h is the width of a computational cell, q is its aspect ratio, and δ_i is the cumulative displacement on point i. The summation is taken over each cell of the fault in order to have the total moment release. In the next step, we compute the derivative of M_0 with respect to time in order to get the moment release rate $\dot{M}_0$ of the fault as a function of time. An example of seismic rupture and the corresponding moment and moment rate curves is presented in Figure 4, showing by the way that the system is, as required, continuous, in the sense that once the rupture nucleated on one asperity; all the cells of the asperity (or belonging to the same group of asperities) break during the same event, so that each cell is not independent of one another. Then, following *Rubin and Ampuero* [2005], *Hillers et al.* [2006], and *Chen and Lapusta* [2009], we consider that an earthquake occurs on the fault each time the sliding velocity and the moment rate reach high enough values, so that elastodynamic effects become dominant. More precisely, we assumed that a seismic event (or seismic rupture) occurred each time $\dot{M}_0$ reaches the threshold $\dot{M}_{0s}$ drawn in Figure 4 and given by the following:

$$\dot{M}_{0s} = \mu \pi R^2 v_s, \tag{12}$$

which would be the moment release rate of one circular asperity of radius R sliding at the threshold velocity v_s. In order to get an estimation of v_s, we follow [*Rubin and Ampuero*, 2005] by setting v_s equal to $v_{dyn} = a\sigma/\eta$; that is, the velocity at which the radiation damping term becomes dominant over the direct effect of rate-and-state friction, so that elastodynamic effects become significant in the system. With our choice of parameters, this approximately leads to v_s = 1 cm s^{-1}. To this point, it is important to notice that a seismic rupture does not necessarily always concern one single asperity: The example of Figure 4 shows a seismic rupture involving several asperities. In the next parts, we will call dynamic sequence such a complex seismic rupture affecting several asperities in the same event. Therefore, one consequence of using a threshold in terms of moment rate is that 10 asperities slipping simultaneously at $v_s/10$ would generate the same moment rate as one asperity slipping at v_s but without radiating any waves. In order to avoid this pitfall, we compare the maximum velocity on the fault to the moment rate to ensure that each event was associated with

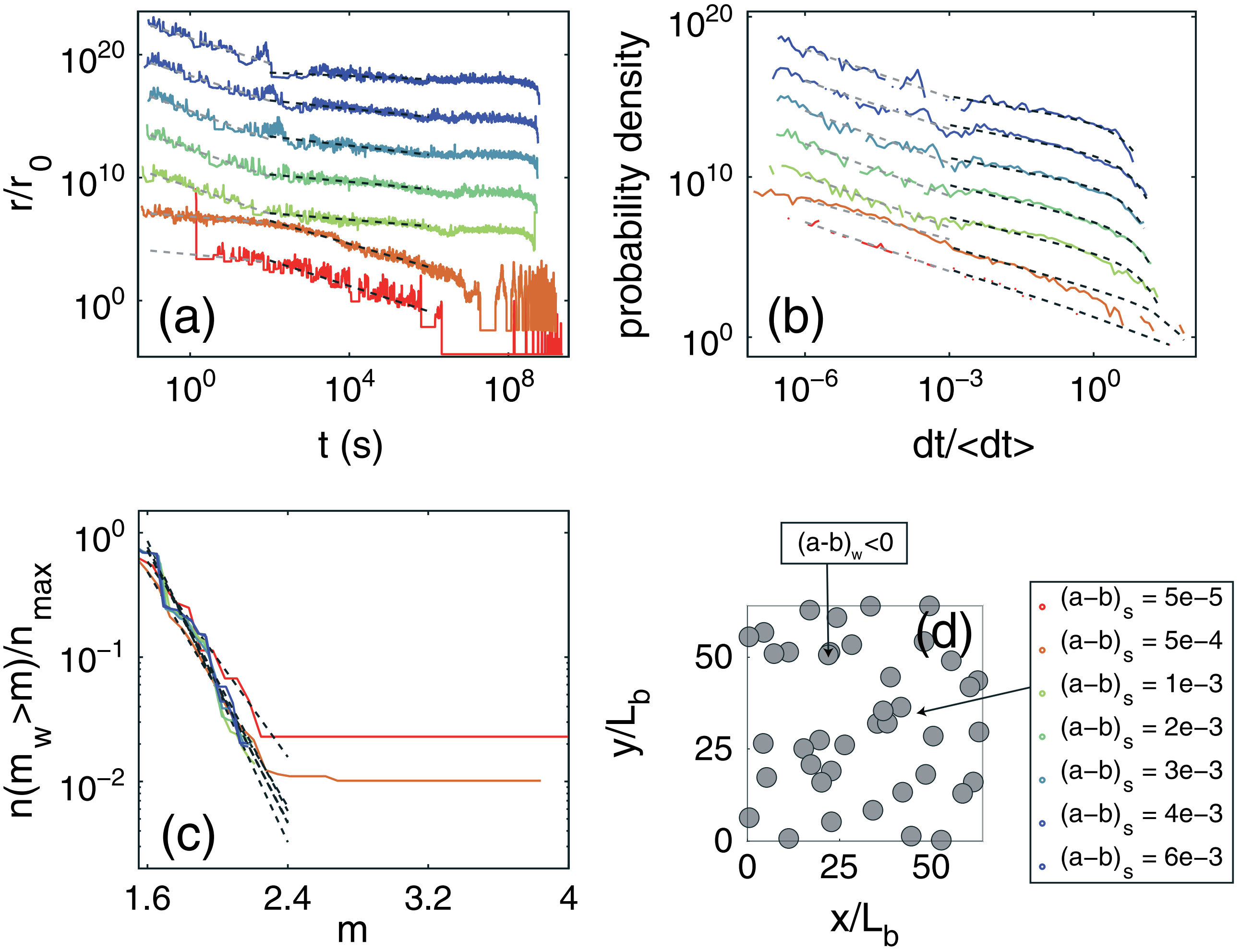

Figure 5. (a) Normalized generalized Omori law for the simulations with a random distribution of 40 asperities. r is the seismicity rate represented as a function of time since the mainshock t, and r_0 is the background seismicity rate. Each color corresponds to a different $(a-b)_s$ friction parameter. For a better visibility, each curve is offset vertically by a constant amount of 10^3. Parameters characterizing the asperities are defined in the text. The gray and black dashed lines are the linear fits for each simulation, before 100 s and between 100 s and 10^6 s, respectively. (b) Normalized interevent time distributions. $< dt >$ is the mean interevent time, and dt is the interevent time. Curves are offset vertically by 10^2 units each time. Colors represent the same parameters as in Figure 5a. Black dashed lines are the gamma functions fitted to the numerical results, and gray dashed lines are the linear fits for $dt/ < dt >$ lower than 10^{-3}. (c) Normalized magnitude-frequency distributions. m and m_w are the moment magnitude, n is the number of earthquakes, and $n_{\max}$ is the maximum number of earthquakes. Parameters are the same as in Figures 5a and 5b. The black dashed lines are the linear fits of the distributions between $m_w = 1.6$ to $m_w = 2.4$. (d) Distribution of weakening asperities ($(a-b)_w < 0$, in gray) on the fault plane.

an episode of high enough slip velocity on the fault. Once we have identified one event, we calculate its seismic moment M_{0e} by computing the cumulative moment during the time of high moment release rate ($\dot{M}_0$ above $\dot{M}_{0s}$), and we converted this moment into magnitude M_w using the relation given by the following [*Kanamori*, 1977]:

$$\log M_{0e} = 1.5M_w + 9.1, \tag{13}$$

where M_{0e} is given in N m. We end up with synthetic catalogs of seismicity generated by our asperity model containing, for each event, its location in space and time, and its moment magnitude. Working on these catalogs, we estimated the same statistics than in the Parkfield case. Usually, we computed catalogs with more than 1500 events occurring after the stabilization phase of the system described in the previous section.

4. Interactions at Different Timescales, Influence of Creep on Clustering

[30] In this section, we created a conceptual heterogeneous fault associating weakening asperities and stable strengthening barriers in order to investigate the relationship

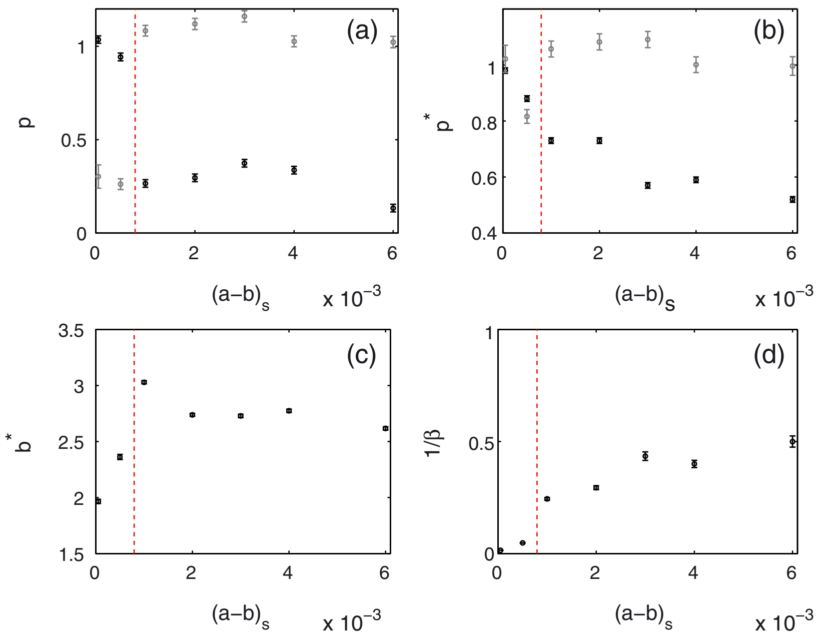

Figure 6. Parameters characterizing the distributions of Figure 5 (gray and black dashed curves) versus anti-asperity friction parameter $(a-b)_s$. (a) Exponent of Omori decay p, (b) exponent of the gamma distribution of interevent delays $p^* = 1 - \gamma$, (c) slope of the magnitude frequency distribution b^*, and (d) $1/\beta$ parameter of the gamma distribution of interevent delays. Gray and black symbols refer respectively to gray and black dashed lines in Figure 5. The error bars where obtained by doing the inversion several times with resampling of the data. The red dashed lines indicate the critical friction parameter $(a-b)_s$ corresponding to the density of asperity $\rho_a = 0.17$ characterizing the random distribution of 40 asperities.

between frictional heterogeneity and statistical properties of seismicity. In particular, we focused on how fault creep interacts with asperities and in which conditions of friction this effect modulates the seismic activity.

[31] To begin with, we generated a random distribution of 40 identical asperities. All the asperities share the same characteristics described in the model parameters section: a radius of 30 m and friction parameters $a_w = 0.001$ and $b_w = 0.005$. The distribution obtained is presented in Figure 5d. By randomly scattering the asperities on the fault, we did not attempt to reproduce the exact picture of seismic asperities represented in Figure 1: Such a distribution would indeed not make too much sense because of the large uncertainty associated with our estimation of the source sizes. However, we tried to reproduce some general characteristics of the asperity distribution at Parkfield, such as the ratio between asperity areas radiating waves and creeping areas. Another important characteristic taken into account in our distribution is the existence of a small variability in the asperity sizes that we obtained by overlapping of the elementary asperities.

[32] Since we were primarily concerned by the role of creeping strengthening barriers between asperities on the seismic activity, we conducted several simulations varying the steady state frictional parameter $(a-b)_s$ of the interasperity areas. For that, we used always the same value of $a_s = 0.007$, and we changed the values of b_s parameter between 0.001 and 0.00695. We also conducted similar experiments with a larger value of a_s, but this had a very little influence on the results reported below. At the end of each simulation, we obtained a synthetic catalog of seismicity, and from this collection of events, we computed the three different statistical distributions mentioned in the second section: generalized Omori distribution, interevent time delays distribution, and magnitude-frequency distribution. The corresponding results are reported in Figure 5. In the following developments, we will first discuss the temporal distributions (Omori and interevent delays) before analyzing the magnitude-frequency distributions.

[33] The generalized Omori distribution and the interevent time delays shown in Figure 5 share the same characteristics: a rapid decay at short time, followed by a more gradual decrease at later times. Moreover, both distributions could be characterized at short timescale by a power law decay, as this has already been mentioned in section 2. At later times, the Omori distribution still exhibits a power-like decay, but this is less obvious for interevent delays. This latter distribution is indeed better characterized by a gamma distribution as this has been formalized by *Hainzl et al.* [2006]. Following the work of these authors, we will therefore assume a probability density function $p(\tilde{dt})$ for the normalized interevent times of the following form:

$$p(\tilde{dt}) = C\tilde{dt}^{\gamma-1}e^{-\tilde{dt}/\beta}, \qquad (14)$$

where $\tilde{dt}$ is the normalized time delay between successive earthquakes, and C, γ, and $1/\beta$ are the parameters of the gamma distribution. To this point, we note that this portion of the interevent times distribution presenting a gamma law shape corresponds to time delays larger than 100 s, and therefore, this is in the range of what could be properly observed in real data such as in the Parkfield area. For that reason, we will in the next parts draw comparison

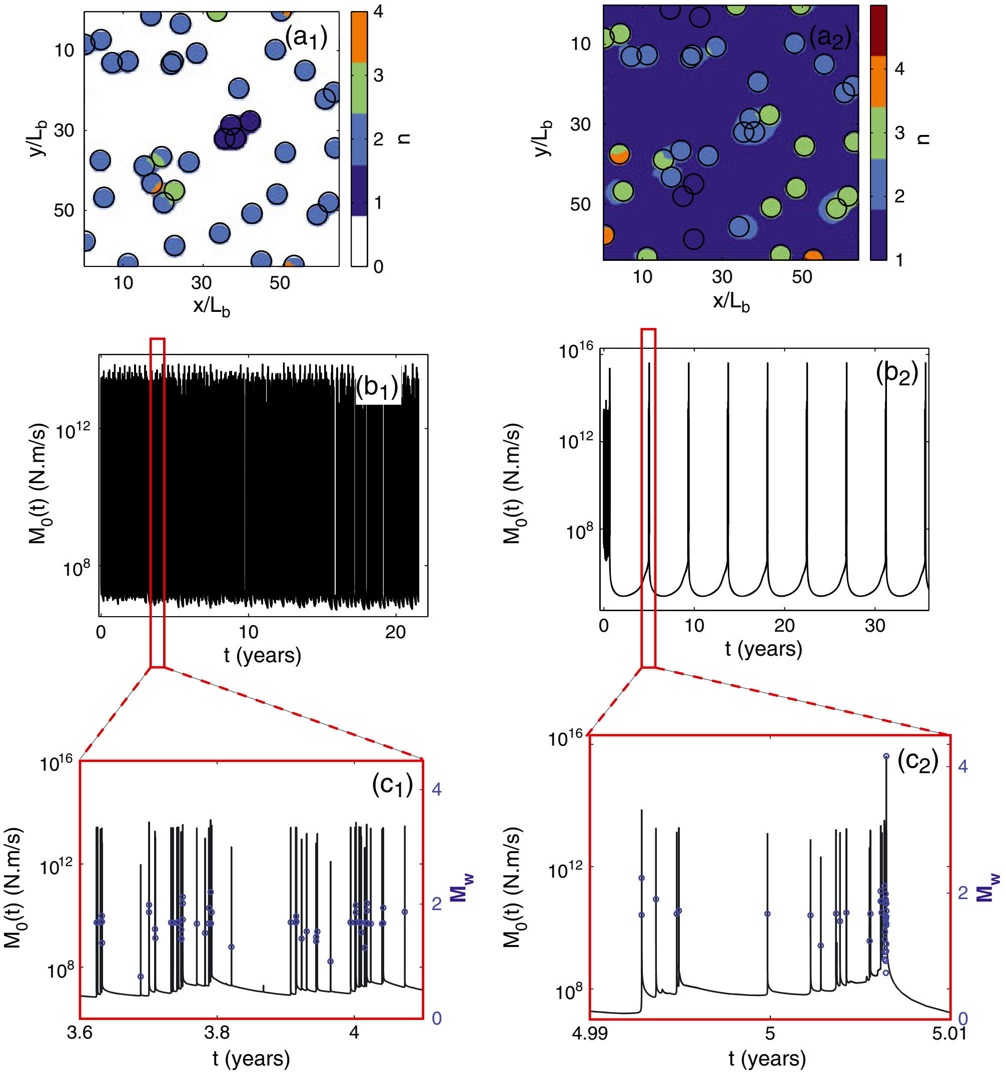

Figure 7. (a) Comparison between frictional asperities (black circles) and seismic asperities (colored areas), for the time period indicated in Figures 7b and 7c, on the fault plane (x,y). The color scale refers to the number n of seismic ruptures occurring during this period of time. (b) Moment release rate $\dot{M}_0$ as a function of time generated by the fault plane. (c) Detail of moment rate evolution (black solid curve), along with magnitude M_w of each event identified (blue points). Seismic asperities of Figures 7a are estimated for the time period represented in Figures 7c. Figures 7a1, 7b1, and 7c1 correspond to a simulation with $(a-b)_s$ = 0.002, whereas Figures 7a2, 7b2, and 7c2 represent a simulation conducted with $(a-b)_s$ = 0.00005.

between $1-\gamma$ and p^* defined previously, and for a matter of simplicity, we will even assimilate p^* to $1-\gamma$. This latter assumption is supported by the asymptotic power law shape of the gamma law for small $\tilde{dt}$.

[34] In order to quantify our results, we computed for each time period the power law exponents of the generalized Omori decay and the power law exponents and gamma parameters ($p^* = 1-\gamma$ and $1/\beta$) of the interevent time distributions. We represented the evolution of these parameters as a function of the interasperity steady state friction $(a-b)_s$ in Figure 6. Doing this, we separated parameters corresponding to short time behavior (in gray) to the one characterizing large time delays (in black), that is larger than 100 s.

[35] The first issue emerging from these results concerns the dependence of all the parameters on $(a-b)_s$, especially in the case of long delays (black symbols in Figure 6). This property is a strong indicator that interasperity creeping segments control the interaction processes between seismic asperities, and in order to interpret those results, one has to consider the critical role of aseismic creep. This creep control is particularly pronounced for interevent time delays, and one possible way to interpret the decay of p^* when $(a-b)_s$ increases is to consider that a larger friction on the creeping segments separating asperities reduces the amount of long term interactions and in turn results in a larger degree of Poissonian and uncorrelated seismicity. Furthermore, the increase of $1/\beta$ parameter with $(a-b)_s$ would imply, according to *Hainzl et al.* [2006], an increase in the background activity relative to mainshock-aftershocks sequences. In other words, asperities are more isolated and

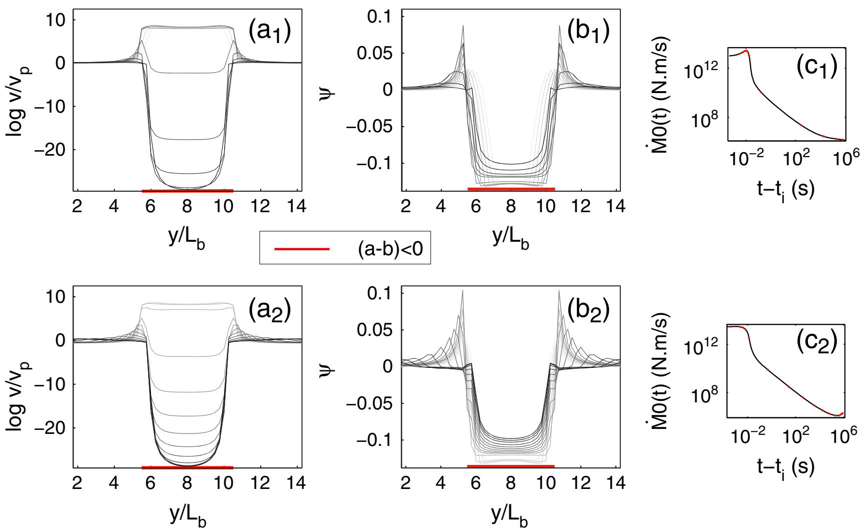

Figure 8. Typical postseismic slip on an asperity. The four profiles represent (a) normalized slip rate v/v_p and (b) normalized stress $\psi = (\tau - \tau_0)/\tau_0$ ($\tau_0 = \mu_0\sigma$) profiles, plotted at instants indicated in the right panels by red crosses. Figures 8a1, 8b1, and 8c1 correspond to an anti-asperity friction parameter of $(a-b)_s = 0.002$, whereas Figures 8a2, 8b2, and 8c2 represent the profiles for $(a-b)_s = 0.0005$. The darkest profiles are the latest in the postseismic relaxation. (c) The insets on the right also indicate the evolution of slip rate at the center of the asperity (black line) as a function of time since the event has nucleated ($t - t_i$). On the profiles, the red line indicates the position of the asperity.

less sensitive to stress perturbations associated with neighboring failures, in the case of large friction parameter $(a–b)_s$. The same conclusion could be deduced from the Omori distribution: The reduction of long term slope with friction parameter $(a-b)_s$ indicates a decrease in the interaction processes driven by fault creep.

[36] Nevertheless, the creep control of interaction processes is less obvious in the case of short term behavior (gray symbols in Figure 6), characterized by power law exponents of the order of one for both Omori decay and interevent time delays. This leads to the conclusion that at short time, less than a hundred of seconds, the asperities interact and stress each other through static processes. In other words, the failure of a source creates stress perturbations on all the neighboring asperities that will in turn accelerate in a similar way than the spring and sliders used by *Dieterich* [1994]. The resulting increase in seismicity is therefore due to the rupture of near to failure asperities on the fault plane, that is asperities loaded enough to break in less than 100 s. According to *Dieterich* [1994], we expect that the slope at short time for both Omori distribution and interevent distribution is controlled by frictional properties of the asperities.

[37] At this point of our analysis, the most significant feature of all the statistical results presented above is probably the abrupt transition in the shape of the distributions that occurs when the friction is lowered from $(a-b)_s = 10^{-3}$ to $(a-b)_s = 5.10^{-4}$. In both Omori and interevent distributions, the slope characterizing long term interaction (at times larger than 100 s from the mainshock, or for $\tilde{dt} > 10^{-3}$) is suddenly increased to values around 1, indicating that strong triggering starts. Furthermore, in the time period between 10^6 s and 10^8 s after each event, the seismicity rates shown in Figure 5a for $(a-b)_s = 5.10^{-4}$ and $(a-b)_s = 5.10^{-5}$ fall at a level smaller than the background level. This corresponds to a period of quiescence preceding the return to the background rate, and this feature is a second characteristics of the transition mentioned. This transition is also very sharp in the magnitude frequency distribution: For large levels of $(a-b)_s$, the magnitudes of the events generated are confined between 1.6 and 2.1, which corresponds to the range of asperity sizes introduced a priori on the fault. As this is shown in Figure 5, the largest asperity created by overlapping is about 5 times larger than a single asperity, and assuming a stress drop of about 6 MPa (Figure 4) in equation (1) leads to a magnitude of 1.64 for the rupture of a single asperity, and to a magnitude of 2.1 for the simultaneous rupture of 5 asperities. For lower friction, some events have magnitudes up to 4, and after making use of equation (1), such a magnitude could only be generated by the seismic rupture of the entire fault, implying a destabilization of the strengthening barriers that accelerate toward seismic velocities.

[38] In order to elucidate the frictional behavior of the fault at this transition, we present in Figure 7a a map of the fault highlighting regions that experienced slip velocities larger than $v_{sis} = 10^{-2}$ m s^{-1}, for two different frictional parameters of the anti-asperity, above the transition (7a1) and below the transition (7a2). In the second case, the entire fault plane has slept one time at high speed, and during this large event, all the asperities were synchronized by this accelerated slip. On the other hand, the absence of color between the asperities in the first case shows that for large frictional strength $(a-b)_s$, only weakening asperities experience seismic sliding velocities, while barriers remain stable or undergo a very limited acceleration. Furthermore, Figure 7b shows that in the regime where the asperities remain isolated without any unstable seismic slip on the creeping barriers, seismic activity is rather independent and uncorrelated, as this was already outlined by the interevent

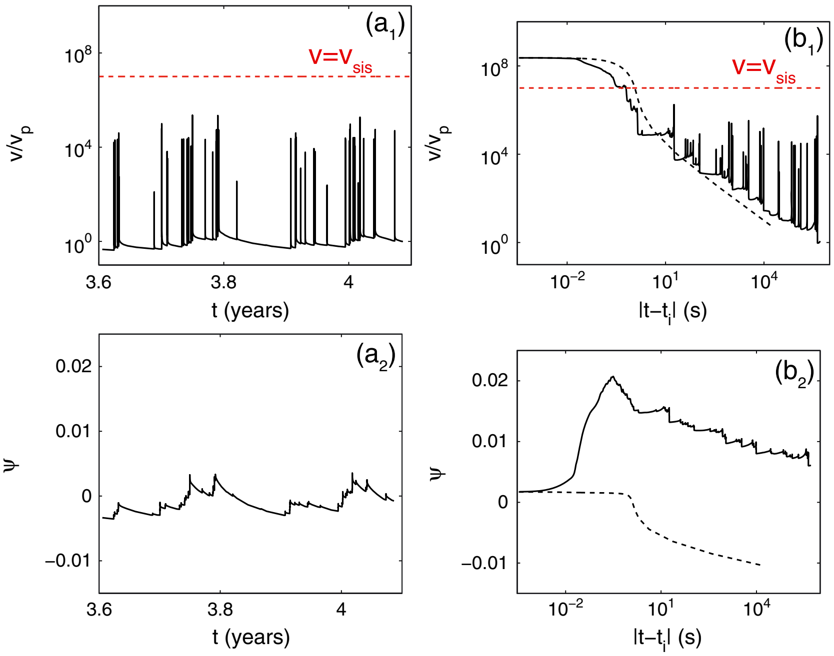

Figure 9. (a1) Mean normalized sliding velocity v/v_p of the anti-asperity (black curve) for the simulation presented in Figures 7a1, 7b1, and 7c1. Red dashed line indicates the seismic threshold v_{sis}. (a2) Mean normalized shear stress $\psi = (\tau - \tau_0)/\tau_0$ ($\tau_0 = \mu_0\sigma$) of the anti-asperity region. (b1 and b2) Same diagrams as Figures 9a1 and 9a2, but for the unstable case presented in Figures 7a2, 7b2, and 7c2, and in a logarithmic timescale. t_i corresponds to the occurrence time of the M_w4 event in Figure 7c2. Black solid curves indicate the pre-M_w4 period, whereas black dashed curves stand for the post-M_w4 period.

time and Omori distributions. On the other hand, the unstable regime is characterized by a strong clustering of activity concentrated in time and followed by long periods of quiescence, resulting in a swarm-like activity that breaks the entire fault in a regular manner. This feature corresponds to the small seismicity rate following the period of intense clustering already mentioned in this analysis of Figure 5a.

[39] With these first simulations, we evidenced a creep control of the long term interactions between asperities, and we showed that this creep control is characterized by two different regimes of interaction depending on the frictional strength of the barriers between asperities: Either isolated asperities that weakly interact to generate an uncorrelated seismic activity or strong interactions that involve the destabilization of the creeping barriers. In the next section, we provide more details about the processes of creep-mediated interaction, and we provide a mechanical interpretation of the transition between the different regimes of activity.

5. Critical Density of Asperities

[40] In order to better constrain the processes characterizing the transition between the two regimes of activity evidenced in the previous section, we present in Figure 8 profiles of velocity and shear stress that characterize the postseismic relaxation following the rupture of an asperity. We represented once again two cases with different frictional strength $(a-b)_s$, either above (profiles 8a1 and 8b1) or below the transition (profiles 8a2 and 8b2). In the two cases, the rupture of the asperity generates a postseismic transient in the velocity strengthening barriers with a region of accelerated sliding and increased shear stress that propagates away from the asperity. This feature has already been shown by *Perfettini and Ampuero* [2008] in the case of a stress perturbation affecting a uniform velocity strengthening fault. The important issue concerning our study of the different regimes of seismic activity is that the postseismic transient is stronger if the friction parameter $(a - b)_s$ is reduced, as this is expected from the analysis of the one-dimensional spring and slider system: In response to a stress step $\Delta\tau$, a velocity strengthening spring and slider characterized by a small enough stiffness accelerates toward a maximum velocity before relaxing back to the steady state corresponding to background loading. The maximum velocity is in this case proportional to $\exp[\Delta\tau/(a-b)_s\sigma]$, and therefore, for some level of forcing $\Delta\tau$, the transient response will be stronger for smaller $(a - b)_s$. Based on these considerations, we propose that in our simulations, the transition between stable and unstable regimes occurs if the strengthening segments accelerate enough in response to the stress perturbations induced by the rupture of the asperities. This model is indeed well supported by the results reported in Figure 7c: The unstable case (low $(a-b)_s$) shows that the M_w4 event occurs at the end of a sequence of smaller earthquakes rupturing isolated asperities or isolated groups of asperities. During this sequence, the mean level of global moment release rate increases progressively at each seismic event, and we interpret this increase as the progressive acceleration of the creeping areas of the fault in response to the successive stress perturbations imposed by the rupture of isolated asperities. The progressive global acceleration on the strengthening barriers for low $(a–b)_s$ values is illustrated in Figure 9b along

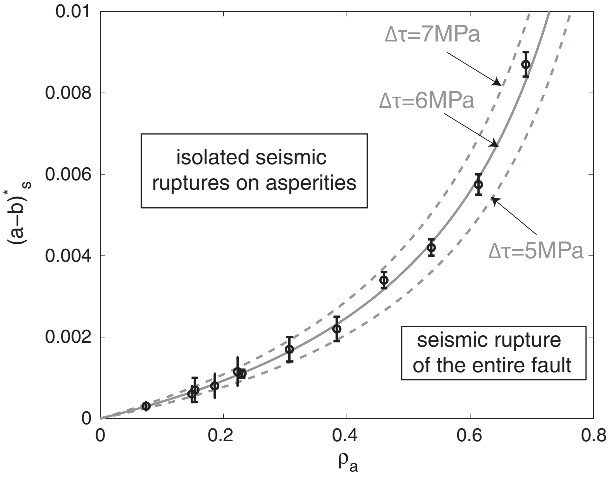

Figure 10. Critical friction parameter $(a-b)^*_s$ of the anti-asperity allowing for the occurrence of events rupturing the entire fault surface at seismic velocities, as a function of asperity density ρ_a defined by expression (15). Black dots are the numerical results, and the gray curves indicate the limit predicted by equation (16) for different values of coseismic stress drop $\Delta\tau_a$ on the asperities. Error bars correspond to the resolution of our sampling of the $(\rho_a,(a-b)_s)$ space. Friction properties characterizing the asperities are the same as in previous sections.

with the global increase in average stress: Each seismic rupture is associated with a stress step that in turn promotes a slip velocity increase. On the other hand, for high values of $(a-b)_s$ (Figure 9a), the mean value of the sliding velocity on the barriers remains stable, essentially because the stress perturbations caused by the seismic events induce a more limited creep acceleration. In other words, if the friction $(a-b)_s$ is sufficiently low, then the creeping barriers between asperities are more sensitive to stress perturbations and become unstable.

[41] In their study of the effect of geological heterogeneity on the characteristic of deformation, *Skarbek et al.* [2012] showed that a transition between aseismic sliding and seismic rupture occurs on a 2-D rate-and-state fault containing both velocity strengthening and velocity weakening material, when the proportion of velocity weakening material in increased above some threshold. Such a transition is in some way comparable to the transition we evidenced, and based on the results of *Skarbek et al.* [2012], we propose that the relative proportion of velocity weakening to velocity strengthening material on our fault is a critical parameter controlling the transition between the two regimes of seismic activity. In the following, we will call this parameter density of asperities ρ_a, and we define it as the ratio between velocity weakening area S_a (that is, the total area covered by asperities) and the total area of the fault plane S so that:

$$\rho_a = \frac{S_a}{S}. \qquad (15)$$

[42] Here, we investigate how the transition between the two regimes identified in our simulations is controlled by ρ_a. For that, we conducted some simulations with multiple asperities varying ρ_a by changing the number of asperities distributed on the fault. The additional asperities had the same characteristics as in the previous section. For each value of ρ_a, we computed the critical value of $(a-b)_s$ below which the system produces episodic large events where creeping portions of fault are destabilized. For that, we used a constant $a_s = 0.007$ and a variable b_s, but also a constant $b_s = 0.001$ and a variable a_s. The results of this study are reported in Figure 10. It appears very clearly that the critical frictional parameter $(a-b)_s$ strongly depends on ρ_a in a very similar way to what is described by *Skarbek et al.* [2012], in the sense that the transition could be described as follows: For some level of $(a-b)_s$ parameter, there is a critical value of ρ_a above which the entire fault slips seismically.

[43] Based on these considerations, we develop in Appendix D some arguments formalized by *Zheng and Rice* [1998] and *Kaneko et al.* [2010] to obtain the relationship between critical $(a-b)_s$ and ρ_a, or in an equivalent way, the dependence of the critical density of asperity ρ_a on the frictional strength of the barriers between asperities $(a-b)_s$. We end up with the following expression, giving for some density of asperities ρ_a, the critical friction parameter $(a-b)^*_s$ leading to unstable slip on the creeping barriers and therefore to connection of the different seismic asperities in a single large event:

$$(a-b)^*_s = \frac{\Delta\tau_a}{\sigma \ln(v_{sis}/v_p)} \frac{\rho_a}{1-\rho_a}, \qquad (16)$$

where $\Delta\tau_a$ is the mean stress drop on one asperity, σ is the normal stress, v_p is the loading rate, and $v_{sis} = 10^{-2}$ m s^{-1} is the value of the threshold sliding velocity defined in the Building Synthetic Catalog section. Inverting equation (16), we obtain the critical density of asperities ρ^*_a for the global destabilization of the system, as a function of friction parameter $(a-b)_s$:

$$\rho^*_a = \left[1 + \frac{\Delta\tau_a}{(a-b)_s \sigma \ln(v_{sis}/v_p)}\right]^{-1}. \qquad (17)$$

[44] Equation (16) predicts a dependence of $(a-b)^*_s$ on ρ_a that is in good agreement with the numerical results as indicated in Figure 10. Furthermore, for the density of asperities characterizing the distribution of Figure 5 ($\rho_a = 0.17$), equation (16) predicts quite well the transition between the two types of statistical distributions as shown by the red dashed lines in Figure 6.

6. Discussion

6.1. Density of Asperities

[45] The rate-and-state asperity model developed in this study allows the mechanical analysis of realistic systems of microseismic sources such as what is inferred in the Parkfield segment of the San Andreas fault. In particular, it has been shown that this numerical approach provides important insights into the relationship between frictional heterogeneity and statistical properties of seismicity. One of the most important goals of our modeling attempt was to study the effect of aseismic sliding on seismic activity. The creep control of seismic activity had already been proposed by *Perfettini and Avouac* [2004] in their analysis of postseismic deformation and aftershock sequence of M_w7.6 1999

Chi-Chi earthquake, *Perfettini et al.* [2005] for the postseismic phase of M_w8.4, 2001, Peru earthquake, as well as *Perfettini et al.* [2007] for the postseismic deformation of M_w7.3, 1992, Landers earthquake. However, these authors did not propose a specific mechanical model of the stressing conditions, as the triggered seismic activity could be located in a sheared volume or broad fault zone and not necessarily concentrated on a single fault plane. The earlier work by *Schaff et al.* [1998] on repeaters within the aftershock sequence of the Loma Prieta earthquake and the more recent study of *Peng and Zhao* [2009] of the migration of early aftershocks of the 2006 Parkfield event are much closer to the mechanics developed in our model. Possibly, one of the most relevant example of creep control of a population of asperities is provided by *Bourouis and Bernard* [2007], as they could properly characterize the overlapping of repeaters (through corner frequency) and moreover have an exceptional, direct in situ access to the total slip on the target fault (through logging before and after the creep event, which was triggered by fluid injection in a 3 km deep borehole). Their conclusion that the Omori law of their triggered seismicity was due to the creep response of the velocity strengthening fault plane, and not to the velocity weakening response of the asperities, is well supported by our simulations in the sense that we obtained a seismic activity strongly modulated by creep.

[46] In our analysis of the influence of creeping barriers on seismicity, we outlined the existence of two regimes of activity depending on the friction strength of the velocity strengthening segments of the fault. In the first one, seismic activity is made of the isolated rupture of asperities (or clusters of asperities) that behave in a quasi-independent manner. In this case, the creeping segments act as strong barriers between asperities and never fail seismically. On the other hand, in the second regime, the rupture of asperities promote a global accelerating transient on the creeping barriers, and if the acceleration is strong enough, then all the asperities are in turn forced to slip together in a major event affecting the entire fault. Moreover, we showed that the transition toward the unstable regime occurs once the density of asperity exceeds some threshold that depends on the frictional strength of the barriers $(a-b)_s$. A similar transition has already been identified by *Skarbek et al.* [2012] who showed that an heterogeneous fault made of a mixture of velocity weakening material and velocity strengthening material produces successively stable sliding, slow slip events and earthquakes as the proportion of velocity weakening material increases. The main difference between the model of *Skarbek et al.* [2012] and the model developed here is that we considered a particular type of velocity weakening material, that is supercritical asperities that always produce seismic events, and consequently, the limit we identified is between two types of seismic events. As a consequence, one could interpret our transition as the transition that would occur in the fault of *Skarbek et al.* [2012] with a higher level of organization. Furthermore, it would be possible to study the transition analyzed in *Skarbek et al.* [2012] using subcritical asperities, leading to the possibility of generating slow slip events. In addition to these aspects, *Skarbek et al.* [2012] demonstrated that their transition strongly depends on velocity weakening parameters as well. Such a dependence should also emerge in our model, in the sense that larger $(a-b)_w$ would give rise according to *Tse and Rice* [1986] to a larger mean stress drop $\Delta\tau_a$ on the asperities, which would decrease the minimum density of asperities necessary to destabilize the entire fault. As a comparison, *Skarbek et al.* [2012] showed that the minimum proportion of velocity weakening material allowing unstable events decreases when the ratio a_w/b_w decreases, which corresponds, in the case of a fixed b_w parameter the same tendency as the one we observe.

[47] The transition between the two different regimes of seismic activity identified in this study is in some way related to the capacity of breaking seismically the barrier between two asperities. This is similar to the conclusion of *Kaneko et al.* [2010] that such interasperity triggering is enhanced for either small barriers or low $(a-b)_s$ parameter. The relation between the theory of *Kaneko et al.* [2010] and the theory presented here could be formulated as follows: for a set of circular asperities of radius R, regularly distributed on a cartesian grid, and separated by strengthening barriers of width d, ρ_a is given locally by the following:

$$\rho_a = \frac{\pi R^2}{(2R+d)^2}, \tag{18}$$

and after re-injecting equation (18) in expression (16), we obtain the critical $(a-b)_s$ of barriers as a function of typical interasperity spacing as follows:

$$(a-b)_s^* = \frac{\Delta\tau_a}{\sigma \ln(v_{sis}/v_p)} \frac{\pi R^2}{[(d+2R)^2 - \pi R^2]}. \tag{19}$$

In the asymptotic case of a small density of asperity ($d >> R$), this expression reduces to the following:

$$(a-b)_s^* = \frac{\pi R^2 \Delta\tau_a}{d^2 \sigma \ln(v_{sis}/v_p)}. \tag{20}$$

Similarly, on a 2-D fault where $\rho_a = 2R/(2R+d)$, we obtain the following:

$$(a-b)_s^* = \frac{2R\Delta\tau_a}{d\sigma \ln(v_{sis}/v_p)}, \tag{21}$$

and the condition for a regime of independent seismicity $(a-b)_s > (a-b)_s^*$ is equivalent to the condition $B > 2$, where B is the nondimensional parameter introduced by *Kaneko et al.* [2010], indicating a probability of crossing the barrier between two asperities equal to zero. Therefore, in our study, we extended the results formalized by *Kaneko et al.* [2010] showing that the same processes govern both the ability of a dynamic rupture to propagate through a stable barrier and the existence of a regime of strongly correlated activity among a population of asperities. The main difference arises from the fact that in the multiple asperity case, some important transients arise without the need to introduce small interasperity distances, if the density of asperities is large enough. In other words, even if one single rupture of asperity will not produce a strong enough perturbation to rupture dynamically the large barriers separating it from its neighbors, the accumulation of a large number of small earthquakes will generate a strong enough perturbation that at the end destabilizes the strengthening barriers between asperities. In this case, the collective effect of all the asperities breaks the barriers, even if a single rupture does not. That is, for instance, the case for the unstable simulation presented in Figures 7a2, 7b2, 7c2, 9b, 8a2, and 8b2, where the main M_w4 event is preceded by small earthquakes occurring on isolated asperities. Note that in Appendix D, we suggest that for smaller values of $(a-b)_s$, a single rupture could break seismically the strengthening barriers. This latter case would correspond to the situation $B = 1$ in the framework developed by *Kaneko et al.* [2010].

[48] As outlined by the comparison between our results and the work of *Kaneko et al.* [2010], our critical density of asperity theory could be used to characterize the stability of velocity strengthening segments between asperities at the larger scale of mega thrust earthquakes in subduction zones. In particular, the great Tohoku-oki earthquake of March 2011 that ruptured a wide portion of the plate interface [*Ammon et al.*, 2011], involved seismic destabilization of creeping segments, and from our model, this observation could be interpreted by a supercritical frictional regime on the plate interface. This assumption is well supported by the simulations of *Kato and Yoshida* [2011] who reproduced the seismic sequence of Tohoku, including small events as well as a large seismic event rupturing seismically 175 km of the up dip plate interface, using a subduction model governed by rate-and-state heterogeneous frictional properties, with two large velocity weakening asperities separated by a small velocity strengthening segment, so that the density of asperity characterizing their plate interface is highly supercritical. The author indeed obtained a mean coseismic slip of 45 m on the main large up dip weakening asperity of their model [see *Kato and Yoshida*, 2011, Figure 4], which corresponds to a stress drop (estimated for a crack of similar dimension) of the order of 60 MPa. According to equation (16) with a mean normal stress of 100 MPa, $\ln(v_{sis}/v_p) \sim 20$, and a density of asperity $\rho_a = 0.4$ on the 175 km long segment of the plate interface that ruptured seismically, this leads to a critical value of $(a-b)_s$ of the order of 0.02, which is much larger than $(a-b)_s \sim 4.10^{-3}$ that characterizes the barrier between the two asperities [see *Kato and Yoshida*, 2011, Figure 2].

6.2. Gutenberg-Richter Distribution

[49] The computation of the magnitude-frequency distributions of our simulated catalogs allowed to identify two distinct mechanisms able to produce some variability in the ratio between the number of small and large earthquakes. The first one is the a priori distribution of source sizes: we recall from the previous sections that the overlapping of some elementary asperities created some variability in the dimensions of the frictional asperities. The second mechanism that creates variability in the magnitudes is the occurrence of unstable accelerated creep that dynamically breaks the barriers between frictional asperities, and allows the fault to rupture in events that are not limited to velocity weakening asperities. Moreover, it has been shown in the previous section that these large events destabilizing the barriers occur once the frictional parameter $(a-b)_s$ of the creeping barriers becomes lower than the critical level associated with the a priori density of frictional asperities. Therefore, we were able to generate reasonable Gutenberg-Richter statistics by generating dynamic cascades rather than by starting from an a priori distribution of source sizes. This is reminiscent of the Gutenberg-Richter law produced by the Burridge and Knopoff spring and slider block model [*Burridge and Knopoff*, 1967].

6.3. Parkfield

[50] In the previous sections, we showed that the two different regimes were characterized by two different kinds of Omori reactivity, two different kinds of interevent time distributions, and two different kinds of magnitude frequency distribution. Therefore, we conclude that the statistical properties of seismicity directly represent the behavior of the creeping segments of fault embedding asperities. More precisely, it is possible to interpret these kinds of statistical distributions in terms of density of asperities. In particular, according to the results of Figure 6, the amount of interaction at long time inferred from the slope of the interevent time distribution (parameter $p^* = 1-\gamma$ of the gamma distribution) could be an indicator of whether the fault is characterized by a subcritical ($p^* \sim 0.5$) or supercritical ($p^* \sim 1$) density of asperities. The same conclusion could be obtained from the analysis of the p parameter of the generalized Omori distribution.

[51] Based on these considerations, we attempt in the following to characterize the activity in Parkfield in terms of density of asperities. In drawing the comparison between our numerical results and the observations in Parkfield, we will exclude the numerical results obtained for time delays smaller than 100 s because, as we mentioned in the second part of this study, we cannot guarantee that the catalog of Parkfield events is complete for time delays smaller than 100 s. Therefore, we will only use the black parameters of Figure 6 characterizing the long term interactions. Drawing the comparison between the observations of Parkfield seismicity reported in Figure 2, showing values of p and p^* of the order of 0.5 to 0.8 in average, and the numerical results presented in Figure 6a and 6b, we would favor a subcritical distribution of sources, which is a small proportion of velocity weakening material on the Parkfield segment of San Andreas Fault, or a supercritical value of $(a-b)_s$ on the barriers between asperities.

[52] However, it seems hard to propose any friction parameter value for the creeping segments of San Andreas Fault based on these results alone, first because this would require to have a precise idea of the density of asperities. In order to partly address this question, we estimated for different regions of the fault an approximate local density of asperity using the location of *Lengliné et al.* [2009] and a rough estimate of the size of the asperities using equation (1). We end up with densities ranging from 0.05 to 0.4, which would result according to equation (16) in a critical friction parameter $(a-b)_s^*$ ranging from 10^{-4} to 1.2×10^{-3} if the assumption of $\Delta\tau_a = 3$ MPa is realistic for the asperities of Parkfield. Therefore, at some places along the fault with high density of asperities (around 0.4), the minimum value of $(a-b)_s$ seems to be as large as 1.2×10^{-3} or larger, if we assume that the regime of seismic activity is globally subcritical. Furthermore, larger values of the stress drop as inferred by *Nadeau and Johnson* [1998] would imply even larger values of $(a-b)_s$, even if at the same time the radius of sources estimated from the seismic moment would be reduced. More precisely, using equation (1) to express the source radius in terms of stress drop $\Delta\tau_a$ and seismic

moment M_{0e}, and reinjecting that result into (19) leads to the following:

$$(a-b)_s^* = \frac{\pi \Delta\tau_a^{1/3}}{\sigma \ln(v_{sis}/v_p)} \left[\left(2\Delta\tau_a^{-1/3} + \frac{d16^{1/3}}{7^{1/3} M_{0e}^{1/3}} \right)^2 - \pi \Delta\tau_a^{-2/3} \right]^{-1}, \tag{22}$$

which is an increasing function of $\Delta\tau_a$ for any value of d and M_{0e}. In particular, in the limit $d >> R$, equation (22) reduces to $(a-b)_s \sim \Delta\tau_a^{1/3}$.

[53] On the other hand, it seems hard to interpret the slope of the magnitude frequency distribution observed in Parkfield with either one or the other regime of activity. Assuming an independent regime suggested by the temporal statistical properties would imply that the distribution is mainly due to the distribution of asperity sizes and not that much a consequence of dynamic cascades involving several asperities. As an alternative way to explain the existence of small values of b^* with large values of $(a-b)_s$ would be to take into account the possibility of triggering by seismic waves. This latter form of triggering would, by the way, certainly lower p^* because small aftershocks would be part of the main rupture resulting in a smaller amount of interaction.

[54] Finally, we end up with a $(a-b)_s$ that at least locally exceeds 0.001. Even if we are not able to provide any better approximation of $(a-b)_s$, these values are clearly larger than what is proposed by *Johnson et al.* [2006] in their estimation of friction parameters governing the afterslip of 2004 Parkfield's earthquake ($(a-b)_s$ between 10^{-4} and 10^{-3}). Since our estimation is based on the analysis of the seismicity occurring before the M_w6 earthquake, we propose as an explanation for this discrepancy that the friction characterizing the creeping segments might have been affected by the stress perturbations induced by the seismic waves of the mainshock, in the sense of a weakening of the contacts. Another possibility would be an elevation of pore fluid pressure that leads to a change in the estimation of $(a-b)_s$ from $(a-b)_s\sigma$. However, we proposed a minimum value for $(a-b)_s$ that is in agreement with the range proposed by *Peng and Zhao* [2009] in their study of the migration of early aftershocks of Parkfield 2004 event. Based on the numerical work of *Kato* [2007], the authors indeed estimated that $(a-b)_s$ should be of the order of 0.001 to 0.004.

6.4. Seismic Quiescence

[55] Another important feature that allows to separate both regimes of seismic activity in the generalized Omori distributions is the occurrence of a seismic quiescence just before the return to the background rate in the unstable regimes shown in Figure 5a. Such periods of low seismic activity have been documented by *Ziv et al.* [2003] at the end of aftershock sequences along the Sargent, Calaveras, and San Andreas Fault in California. However, the quiescence observed in our synthetic statistical distributions is related to the long periods without any seismic event separating the seismic swarms in the unstable regime, as shown in Figure 7b, and we believe that these quiescent periods are mainly an artifact of the periodic geometry we adopted. The repetition of an identical finite fault plane indeed prevents a seismic rupture to stop once it has reached the boundaries of the fault. Consequently, the seismic sequence detailed in Figure 7c2 is similar to a swarm that develops itself until the occurrence of a large unbounded event that artificially stops the swarm, the system looses its mechanical memory, and from this point, the simulation does not make any physical sense. On natural faults, all the events of a swarm would have a finite extent, and the swarm would die in a different way. This artificial feature might not be consistent with real observations.

6.5. Modeling Microseismic Processes

[56] One way to improve the characterization of the microseismic source friction properties in multiplet prone areas would be the systematic calculation of source parameters, such as corner frequency in order to obtain a more precise estimation of source size. Another way would be to relax the constraint of source overlapping in the definition of multiplets for the relocation, to test the stability of the seismic asperities observed in Figure 1. Starting from a better picture of how seismic asperities are distributed on the fault plane could help in the modeling of processes of interaction, in the perspective of quantifying local friction parameters from statistical observations.

[57] Furthermore, we were not able to draw any satisfying conclusion from the evaluation of b^* values of the magnitude-frequency distributions about the frictional heterogeneity at Parkfield. This arises because the magnitude-frequency distribution is not only modulated by the relative proportion between weakening material and strengthening material as the other event statistics seem to be but it is also strongly controlled by the distribution of asperity sizes (explaining the slope obtained in Figure 5c between M_w = 1.6 and M_w = 2.4), and we did not, in this study, investigate different kinds of distribution of source sizes. This issue requires more attention and would be of great interest for the understanding of frictional behavior of multiplet prone areas such as Parkfield. In other words, if the temporal statistical distributions allow to quantify the density of asperities, then one could develop a complementary method allowing to address the question of the spatial organization and sizes of the velocity weakening asperities from the analysis of the magnitude-frequency distributions.

[58] Moreover, our model is limited in the sense that we neglected more complex processes such as fluid diffusion, thermal pressurization, considered for instance by *Segall and Rice* [2006] or fully dynamic aspects of rupture including elastic waves taken into account by *Chen and Lapusta* [2009], that might play an important role in the physics of earthquake interactions.

[59] Finally, the processes of interaction and the notion of critical density that we analyzed in this study do not depend on the scale of the asperities, meaning that our results would apply in the case of larger repeaters, such as what is observed in subduction zones, but also in the case of tremor activity.

7. Conclusion

[60] We have presented a continuous rate-and-state 3-D model of asperities, coupling seismic and aseismic behavior, which allows for the computation of synthetic catalogs that could be studied with the same statistical methods as for real catalogs. In particular, we showed that our model reproduces reasonable earthquake statistics, including generalized Omori decay, interevent time distribution, and Gutenberg-Richter statistics. Moreover, by analyzing a series of

simulations with a simple distribution of asperities, we outlined the importance of the creeping barriers in the processes of interactions among a population of sources. Furthermore, we characterized different regimes of interaction in terms of a new concept of critical density of asperities, and therefore, we provided a way to interpret statistical properties of seismicity in terms of frictional heterogeneity on faults. Based on this concept of critical density of asperities, we applied our numerical model to the understanding of the friction properties of the Parkfield segment of San Andreas Fault during the period preceding the 2004 M_w earthquake, resulting in values for $(a-b)_s$ in the upper range of what has been recently proposed for the postseismic period. Although our model lacks some important physics related to fault systems such as fluid diffusion, thermal effects, and wave effects, we were able to analyze some important insights into the processes of seismic source interaction in general, since we developed concepts applicable to microseismic and tremor activity as well as to larger earthquakes.

Appendix A: Elastic Interaction in a Finite Medium

[61] The Green function used by *Maruyama* [1964] to compute the elastic kernel k_{ij} of equation (8) is the Green function for an elastic half space, and therefore, the use of a finite geometry in which the slip rate is controlled at a distance $w/2$ from the fault plane introduces some error in the estimation of the elastic interactions. To quantify this effect, we consider the simplified antiplane 2-D situation that approximately accounts for the slip profiles during a seismic cycle involving a single velocity-weakening asperity. In this 2-D model, the fault situated at $y = 0$ separates two elastic slabs of thickness $w/2$, and the only nonvanishing component of displacement is in the z direction. We impose the displacement $\delta(x)$ at $y = 0$ in the form of a standing wave of amplitude Δu so that we have:

$$\delta(x) = \Delta u \cos(kx). \tag{A1}$$

with $k = 2\pi/L$, L being the size of the fault plane. Following *Horowitz and Ruina* [1989] in this finite geometry, slip $\delta(x)$ and shear stress $\tau(x)$ on the fault are related in the following way:

$$\tau(x) = -\frac{\mu|k|}{2\tanh(|k|w/2)}\delta(x). \tag{A2}$$

Alternatively, in the case of a semi-infinite elastic half space, we have the following:

$$\tau_\infty(x) = -\frac{\mu|k|}{2}\delta(x), \tag{A3}$$

where $\tau_\infty(x)$ refers to the shear stress on the $y = 0$ in the semi-infinite geometry. Thus, the ratio between the amplitude of the stress wave $\Delta\tau$ in each geometry is the following:

$$\frac{\Delta\tau}{\Delta\tau_\infty} = \frac{1}{\tanh(|k|w/2)} = \frac{1+e^{-|k|w}}{1-e^{-|k|w}}, \tag{A4}$$

and the error ϵ in shear stress introduced in our simulations by the finite geometry becomes:

$$\epsilon = \left|1 - \frac{\Delta\tau}{\Delta\tau_\infty}\right| = \frac{2e^{-|k|w}}{1-e^{-|k|w}}. \tag{A5}$$

With $L = 768$ m and $w = 3$ km, we obtain $\epsilon = 4.10^{-11}$, showing that $\epsilon << 1$, so that the error introduced by the use of a Green function of the elastic half space for our finite geometry is negligible. Furthermore, the value ϵ given above is slightly over estimated because we considered the largest possible wavelength of a slip profile over the fault considered, and because stress decays more rapidly in a 3-D medium than in 2-D.

Appendix B: Normalized Differential System for the Asperity Model

[62] In this section, we present the system of first-order differential equations to be solved in the rate-and-state asperity model. In the main text, we showed that equation (10), together with the aging state evolution law (3) constitute a set of first-order differential equations for the evolution of v_i and Θ_i at each grid point i of the fault. In order to identify the main nondimensional parameters controlling the evolution of the fault, we will define normalized quantities and rewrite the differential system in terms of the normalized quantities.

[63] Normalization has been done in the following way, where quantities with a star * designate normalized quantities:

$$\begin{cases} t^* = tv_p/d_c \\ v_i^* = v_i/v_p \\ \sigma^* = \sigma/\eta v_p \\ k_{ij}^* = k_{ij}d_c/\eta v_p \\ \Theta_i^* = \Theta_i, \end{cases} \tag{B1}$$

where d_c is the critical slip of the rate-and-state friction law, v_p is the imposed loading rate, and η is the damping parameter. Therefore, the differential system becomes the following, in terms of the nondimensional quantities:

$$\begin{cases} \dot{v}_i^* = \dfrac{v_i^*}{v_i^* + a_i\sigma^*}\Big[-\beta(v_i^*-1) + \sum_j k_{ij}^*(v_j^*-1) \\ \qquad\qquad + b_i\sigma^*(v_i^* - e^{-\Theta_i^*})\Big] \\ \dot{\Theta}_i^* = e^{-\Theta_i^*} - v_i^* \quad , \end{cases} \tag{B2}$$

where dots refer to the differentiation with respect to normalized time t^*, $\beta = \mu d_c/\eta v_p w$ is a nondimensional parameter corresponding to the imposed motion at a distance w from the fault, and $(i,j) \in \{1,\ldots,N\}^2$, with N being the number of grid points on the fault. We end up with the system (B2), made of $n = 2N$ first-order differential equations giving the evolution of the sliding velocity v and state variable Θ through time on each point of the fault. Furthermore, the relevant nondimensional parameters that remain in (B2) are β, σ^*, a, and b friction parameters that will be of two types: either velocity weakening ($a - b < 0$) or velocity strengthening ($a - b > 0$).

Appendix C: Time Step Control

[64] In this section, we present the method used to control the time step in the Runge-Kutta algorithm implemented to solve the differential system (B2). In the rest of Appendix C, all the quantities will be nondimensional quantities defined in Appendix B, and for the sake of simplicity, we will omit the star * in their notation. In order to limit the amplification of the numerical error, the ratio between the time step and the amplitude of the largest magnitude eigenvalue of the

linearized differential system associated with (B2) has to be smaller than one, that is, as follows:

$$\frac{\Delta t}{\max\left(|\lambda_i|, i \in \{1, \ldots, n\}\right)} < 1, \tag{C1}$$

where Δt is the time step, λ_i is the ith eigenvalue of the linearized differential system associated with (B2), and n is the dimension of the system. Therefore, we choose the time step as being:

$$\Delta t = \frac{1}{\lambda_m}, \tag{C2}$$

where $\lambda_m = \max\left(|\lambda_i|, i \in \{1, \ldots, n\}\right)$, and the adaptation of Δt requires the computation of the largest magnitude eigenvalue of J, the jacobian matrix associated with the linearized system of n differential equations. In our case, the system of differential equations (B2) is of the following form:

$$\begin{cases} \dot{v}_i & = f_i(v_1, v_2, \ldots, v_N, \Theta_1, \Theta_2, \ldots, \Theta_N) \\ \dot{\Theta}_i & = g_i(v_1, v_2, \ldots, v_N, \Theta_1, \Theta_2, \ldots, \Theta_N), \end{cases} \tag{C3}$$

where N is the number of grid points, and $i \in \{1, .., N\}$. Thus, the Jacobian matrix J associated with B2 has the following form:

$$J = \begin{pmatrix} A & B \\ C & D \end{pmatrix}, \tag{C4}$$

where A, B, C, and D are the square matrices of size N by N, which respective coefficients a_{ij}, b_{ij}, c_{ij}, and d_{ij}, $(i,j) \in \{1, .., N\}^2$, are given by the following:

$$a_{ij} = \frac{\partial f_i}{\partial v_j} = \left\{ \frac{v_i}{v_i + a_i\sigma}\left[-\beta + k_{ii} + b_i\sigma\right] + \frac{a_i\sigma}{v_i(v_i + a_i\sigma)} f_i \right\} \delta_{ij} + \frac{v_i k_{ij}}{v_i + a_i\sigma}(1 - \delta_{ij}), \tag{C5}$$

$$b_{ij} = \frac{\partial f_i}{\partial \Theta_j} = \frac{b_i v_i \sigma}{v_i + a_i\sigma} e^{-\Theta_i}\delta_{ij}, \tag{C6}$$

$$c_{ij} = \frac{\partial g_i}{\partial v_j} = -\delta_{ij}, \tag{C7}$$

$$d_{ij} = \frac{\partial g_i}{\partial \Theta_j} = -\delta_{ij} e^{-\Theta_i}, \tag{C8}$$

where δ_{ij} is the Kronecker symbol, and f_i is equal to the acceleration $\dot{v}_i$ of the grid point i and is defined in (B2). The computation of the largest magnitude eigenvalues of J is performed by an implicitly restarted Arnoldi iteration [*Arnoldi*, 1951] and *Sorensen* [1992] on J using the Arnoldi Package ARPACK developed by *Lehoucq et al.* [1998]. We present in Figure C1 an example of the eigenvalue computation in the case of a single asperity identical to the one used in our multiple asperities simulations, surrounded by a creeping region with different friction properties in the range of what we have used in this study. The main feature emerging from this figure is the strong correlation between amplitude of the largest magnitude eigenvalue and the maximum normalized sliding velocity v_m on the fault plane. However, this method is rather time consuming in the case of multiple asperities situations that require a large number of grid points and is in practice difficult to implement. In order to simplify the estimation of the time step, we therefore used the correlation between λ_m and v_m outlined in Figure C1, arguing that whatever friction characterizes the creeping segments on the fault, λ_m is always smaller than kv_m^{α}, k being a constant estimated through the full computation in the single asperity case, and according to equation (C2), we compute the time step Δt from the maximum sliding velocity on the fault plane as follows:

$$\Delta t = \frac{1}{k} v_m^{-\alpha}. \tag{C9}$$

In this study, we used $k = 20$ and $\alpha = 1$ according to the results shown in Figure C1. This method gives an overestimation of λ_m and therefore an underestimation of Δt for some parts of the seismic cycle on the asperity, ensuring that condition C1 is still valid, and therefore that the error amplification remains bounded. Finally, in order to test the stability of the solutions, we also conducted selected simulations with smaller time steps (with $k = 40$) that did not affect the results. In particular, the main statistical features of the synthetic catalogs remained stable.

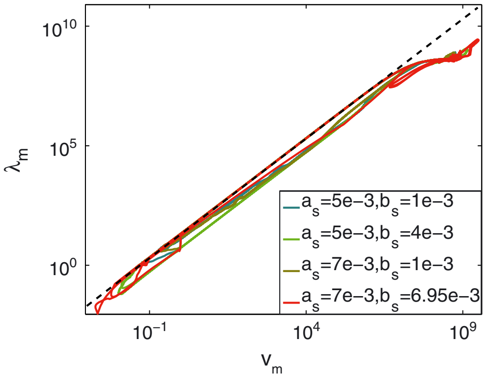

Figure C1. Normalized amplitude (λ_m) of the largest magnitude eigenvalue of the linearized system associated with (B2) versus maximum normalized sliding velocity v_m on the fault during the seismic cycle generated by a single circular velocity weakening asperity surrounded by fault creep and loaded at constant rate. The asperity is identical to the ones used in the multiple asperities simulations, with $R = 30$ m, $a_w = 0.001$, and $b_w = 0.005$. Each different color represents different friction parameters a_s and b_s on the anti-asperity. The black dashed line corresponds to the linear dependence of λ_m on v_m: $\lambda_m = 20v_m$.

Appendix D: Critical Density of Asperities Allowing Unstable Slip of the Strengthening Barriers

[65] In this section, we focus on the case of a fault containing both velocity weakening asperities and velocity strengthening areas, and we derive the critical proportion of velocity weakening material (or critical density of asperities) allowing seismic events that rupture dynamically the entire fault. The necessary condition for such events to occur is to make creeping segments accelerate up to seismic velocities. Furthermore, we have observed in our simulations that such acceleration occurs when the density of velocity weakening asperities is large enough on the fault. Therefore, we want to find the minimum density of asperities allowing acceleration.

[66] Starting from the velocity-strengthening spring block model, *Perfettini and Ampuero* [2008] showed that a velocity-strengthening fault subjected to a positive stress

perturbation $\Delta\tau_s$ affecting an area much larger than L_b will undergo a creep transient that first accelerates, then relaxes to the background loading velocity. The fault, if obeying aging state evolution law, initially creeping at v_p, reaches after acceleration the maximum sliding velocity $v_{\max}$ given by the following:

$$v_{\max} = v_p \exp\left[\frac{\Delta\tau_s}{(a-b)_s\sigma}\right]. \tag{D1}$$

Considering that velocity strengthening barriers between asperities creeping at v_p roughly behave like the spring block in response to a stress perturbation, we deduce from equation (D1) that the creeping portions of the fault will accelerate toward the seismic velocity v_{sis} if the coseismic stress perturbation $\Delta\tau_s$ associated with the rupture of the asperities is on average larger than $\Delta\tau_s^*$ given by the following:

$$\Delta\tau_s^* = (a-b)_s\sigma \ln\frac{v_{sis}}{v_p}. \tag{D2}$$

Therefore, equation (D2) provides the critical average stress perturbation allowing the seismic rupture of velocity strengthening segments. This critical threshold depends on the steady state velocity-strengthening friction parameter $(a-b)_s$, and equation (D2) could be written in a different way as follows:

$$(a-b)_s^* = \frac{\Delta\tau_s}{\sigma\ln(v_{sis}/v_p)}, \tag{D3}$$

showing that for some level of stress perturbation $\Delta\tau_s$, there is a critical value of $(a-b)_s$ called $(a-b)_s^*$ allowing large acceleration to develop in velocity strengthening segments. In a second time, we need to estimate the link between $\Delta\tau_s$ and the average stress drop on asperities $\Delta\tau_a$. To do that, we use the result first derived by *Zheng and Rice* [1998] in the elastodynamic case and further used by *Kaneko et al.* [2010] to develop their condition allowing a seismic rupture to propagate through a velocity strengthening barrier. According to the expression of quasi-dynamic stress (8), the stress on the fault plane is of the following form:

$$\tau(\mathbf{x},t) = \tau^* + f(\mathbf{x},t) - \eta v(\mathbf{x},t), \tag{D4}$$

where τ^* is the stress acting on the fault in the absence of displacement, f represents the effect of elastic interactions at point $\mathbf{x} = (x,y)$ and time t due to differential slip on the fault, and ηv is the radiation damping term. Following the derivation of *Zheng and Rice* [1998] and *Geubelle and Rice* [1995] in the elastodynamic case, it could be shown that in the case of static interactions, the integral of f over the entire fault surface S vanishes. Therefore, integrating equation (D4) leads to the following property:

$$\int\int_S [\tau(\mathbf{x},t) - \tau^*]\mathrm{d}S - \eta\int\int_S v(\mathbf{x},t) = 0. \tag{D5}$$

According to *Kaneko et al.* [2010], as long as the sliding velocity is small enough, the second term in (D5) can be neglected. Assuming that this is the case before and after a seismic event, we end up with the following equality:

$$\int\int_S [\tau_2-\tau_1]\mathrm{d}S = \int\int_{S_a}[\tau_2-\tau_1]\mathrm{d}S + \int\int_{S_s}[\tau_2-\tau_1]\,\mathrm{d}S = 0, \tag{D6}$$

where τ_2 and τ_1 respectively refer to the shear stress after and before the earthquake, S_a is the velocity weakening area (asperities), and S_s is the velocity strengthening area. This last results indicates that the stress drop integrated over the velocity weakening asperities balances the stress perturbation integrated over the velocity strengthening area. Considering the average stress variations, equation (D6) leads to the following:

$$S_a\Delta\tau_a = S_s\Delta\tau_s = (S - S_a)\Delta\tau_s, \tag{D7}$$

where $\Delta\tau_a$ is the mean value of the stress drop $\tau_1 - \tau_2$ on one asperity, $\Delta\tau_s$ is the average stress increase $\tau_2 - \tau_1$ over the velocity strengthening area, and S is the total area of the fault. The ratio of velocity weakening area S_a over total area S is the density of asperity ρ_a as defined by equation (15), and we end up with the following relation between $\Delta\tau_s$ and $\Delta\tau_a$:

$$\Delta\tau_s = \frac{\rho_a}{1-\rho_a}\Delta\tau_a. \tag{D8}$$

In our derivation of (D7) and (D8), we have assumed that all the asperities have ruptured, and therefore, $\Delta\tau_s$ is the maximum average stress perturbation that could experience the strengthening barriers on the fault. Re-injecting equation (D8) into (D3) leads to the following expression of $(a-b)_s^*$, as a function of the density of asperity:

$$(a-b)_s^* = \frac{\Delta\tau_a}{\sigma\ln(v_{sis}/v_p)}\frac{\rho_a}{1-\rho_a}. \tag{D9}$$

One could rearrange equation (D9), to get, for a given stress drop $\Delta\tau_a$ on the asperities and a given friction parameter $(a-b)_s$ the critical density of asperities ρ_a^* allowing dynamic rupturing of the stable strengthening segments. Thus, from equation (D9), we have the following:

$$\rho_a^* = \left[1 + \frac{\Delta\tau_a}{(a-b)_s\sigma\ln(v_{sis}/v_p)}\right]^{-1}. \tag{D10}$$

If we relax the assumption that the ruptures of all the asperities contribute to $\Delta\tau_s$, we end up with a smaller mean stress perturbation on the strengthening segments of the fault, and the transition between the two regimes occurs at a lower $(a-b)_s^*$ for a given density of asperity. Therefore, we expect to have as many destabilizing transitions as asperities on the fault: The most unstable regime would appear for a value of $(a-b)_s$ small enough to allow the rupture of a single asperity to destabilize the entire fault. In this framework, equations (D9) and (D10) indicate the first global destabilization that occurs in a multiple asperity system that evolves in the $((a-b)_s, \rho_a)$ space from a stable situation with an independent regime of seismicity.

[67] **Acknowledgments.** This work was supported by the École Normale Supérieure grant, the seismological laboratory of the IPG Paris, and by the ANR project ASEISMIC. It is also integrated in the European program REAKT. We would like to thank 0. Lengline and D. Marsan who kindly provided their relocation catalog of Parkfield events. We thank the Associate Editor and two anonymous reviewers for providing comments that significantly improved the manuscript. We also thank Raúl Madariaga, Harsha S. Bhat, Jean-Pierre Vilotte, and Alexandre Schubnel for discussions.

References

Ammon, C. J., T. Lay, H. Kanamori, and M. Cleveland (2011), A rupture model of the 2011 off the Pacific coast of Tohoku earthquake, *Earth Planets Space*, *63*(7), 693.

Ampuero, J., and A. Rubin (2008), Earthquake nucleation on rate and state faults: Aging and slip laws, *J. Geophys. Res.*, *113*, B01,302, doi:10.1029/2007JB005082.

Ariyoshi, K., T. Matsuzawa, J. Ampuero, R. Nakata, T. Hori, Y. Kaneda, R. Hino, and A. Hasegawa (2012), Migration process of very low-frequency events based on a chain-reaction model and its application to the detection of preseismic slip for megathrust earthquakes, *Earth Planets Space*, *64*(8), 693–702.

Arnoldi, W. (1951), The principle of minimized iterations in the solution of the matrix eigenvalue problem, *Quart. J. Applied Mathematics*, *9*, 17–29.

Bouchon, M., H. Karabulut, M. Aktar, S. Özalaybey, J. Schmittbuhl, and M. Bouin (2011), Extended nucleation of the 1999 Mw 7.6 Izmit earthquake, *Science*, *331*(6019), 877.

Bourouis, S., and P. Bernard (2007), Evidence for coupled seismic and aseismic fault slip during water injection in the geothermal site of Soultz (France), and implications for seismogenic transients, *Geophys. J. Int.*, *169*(2), 723–732.

Bürgmann, R., D. Schmidt, R. Nadeau, M. d'Alessio, E. Fielding, D. Manaker, T. McEvilly, and M. Murray (2000), Earthquake potential along the northern Hayward Fault, California, *Science*, *289*(5482), 1178–1182.

Burridge, R., and L. Knopoff (1967), Model and theoretical seismicity, *B. Seismol. Soc. Am.*, *57*(3), 341–371.

Chen, T., and N. Lapusta (2009), Scaling of small repeating earthquakes explained by interaction of seismic and aseismic slip in a rate and state fault model, *J. Geophys. Res.*, *114*, B01,311, doi:10.1029/2008JB005749.

Dieterich, J. (1994), A constitutive law for rate of earthquake production and its application to earthquake clustering, *J. Geophys. Res.*, *99*, 2601–2618.

Dieterich, J. (1995), Earthquake simulations with time-dependent nucleation and long-range interactions, *Nonlinear Proc. Geoph.*, *2* (3/4), 109–120.

Dieterich, J. H. (1979), Modeling of rock friction-1. Experimental results and constitutive equations, *J. Geophys. Res.*, *84*, 2161–2168.

Dieterich, J. H. (1992), Earthquake nucleation on faults with rate and state-dependent strength, *Tectonophysics*, *211*, 115–134.

Dreger, D., R. Nadeau, and A. Chung (2007), Repeating earthquake finite source models: Strong asperities revealed on the San Andreas Fault, *Geophys. Res. Lett.*, *34*, L23,302, doi:10.1029/2007GL031353.

Geubelle, P. H., and J. R. Rice (1995), A spectral method for three-dimensional elastodynamic fracture problems, *J. Mech. Phys. Solids*, *43*(11), 1791–1824, doi:10.1016/0022-5096(95)00043-I.

Gutenberg, B., and C. Richter (1956), Earthquake magnitude, intensity, energy and acceleration, *Bull. Seism. Soc. Am.*, *46*, 105–145.

Hainzl, S., F. Scherbaum, and C. Beauval (2006), Estimating background activity based on interevent-time distribution, *B. Seismol. Soc. Am.*, *96*(1), 313–320.

Harris, R., and P. Segall (1987), Detection of a locked zone at depth on the Parkfield, California, segment of the San Andreas Fault, *J. Geophys. Res.*, *92*(B8), 7945–7962.

Helmstetter, A., and D. Sornette (2002), Diffusion of epicenters of earthquake aftershocks, Omoris law, and generalized continuous-time random walk models, *Phys. Rev. E*, *66*(6), 061,104.

Hillers, G., Y. Ben-Zion, and P. Mai (2006), Seismicity on a fault controlled by rate-and state-dependent friction with spatial variations of the critical slip distance, *J. Geophys. Res.*, *111*(B1), B01,403.

Horowitz, F. G., and A. Ruina (1989), Slip patterns in a spatially homogeneous fault model, *J. Geophys. Res. (1978–2012)*, *94*(B8), 10,279–10,298.

Igarashi, T., T. Matsuzawa, and A. Hasegawa (2003), Repeating earthquakes and interplate aseismic slip in the northeastern Japan subduction zone, *J. Geophys. Res.*, *108*(10.1029), 2002.

Johnson, K., R. Bürgmann, and K. Larson (2006), Frictional properties on the San Andreas Fault near Parkfield, California, inferred from models of afterslip following the 2004 earthquake, *B. Seismol. Soc. Am.*, *96*(4B), S321–S338.

Kagan, Y., and L. Knopoff (1981), Stochastic synthesis of earthquake catalogs, *J. Geophys. Res.*, *86*(B4), 2853–2862.

Kagan, Y., and L. Knopoff (1987), Statistical short-term earthquake prediction, *Science*, *236*(4808), 1563–1567.

Kanamori, H. (1977), The energy release in great earthquakes, *J. Geophys. Res.*, *82*(20), 2981–2987.

Kaneko, Y., J. Avouac, and N. Lapusta (2010), Towards inferring earthquake patterns from geodetic observations of interseismic coupling, *Nat. Geosci.*, *3*(5), 363–369.

Kato, N. (2003), Repeating slip events at a circular asperity: Numerical simulation with a rate-and state-dependent friction law, *Bull. Earthq. Res. Inst.*, *78*, 151–166.

Kato, N. (2004), Interaction of slip on asperities: Numerical simulation of seismic cycles on a two-dimensional planar fault with nonuniform frictional property, *J. Geophys. Res.*, *109*(B12), B12,306.

Kato, N. (2007), Expansion of aftershock areas caused by propagating postseismic sliding, *Geophys. J. Int.*, *168*(2), 797–808.

Kato, N., and S. Yoshida (2011), A shallow strong patch model for the 2011 great Tohoku-oki earthquake: A numerical simulation, *Geophys. Res. Lett.*, *38*(7) L00G04, doi:10.1029/2011GL048565.

Lehoucq, R., D. Sorensen, and C. Yang (1998), *ARPACK Users' Guide: Solution of Large-Scale Eigenvalue Problems With Implicitly Restarted Arnoldi Methods*, vol. 6, Siam, Philadelphia, Pa.

Lengliné, O., et al. (2009), Inferring the coseismic and postseismic stress changes caused by the 2004 Mw= 6 Parkfield earthquake from variations of recurrence times of microearthquakes, *J. Geophys. Res.*, *114*, B10,303.

Marone, C. (1998), Laboratory-derived friction laws and their application to seismic faulting, *Annu. Rev. Earth Pl. Sc.*, *26*(1), 643–696.

Marsan, D., and O. Lengline (2008), Extending earthquakes' reach through cascading, *Science*, *319*(5866), 1076–1079.

Maruyama, T. (1964), 16. Statical elastic dislocations in an infinite and semi-infinite medium, *Bull. Earthq. Res. Inst.*, *42*, 289–368.

Matsuzawa, T., T. Igarashi, and A. Hasegawa (2002), Characteristic small-earthquake sequence off Sanriku, northeastern Honshu, Japan, *Geophys. Res. Lett.*, *29*(11), 1543, doi:10.1029/2001GL014632.

Molchan, G. (2005), Interevent time distribution in seismicity: A theoretical approach, *Pure Appl. Geophys.*, *162*(6), 1135–1150.

Murray, J., P. Segall, P. Cervelli, W. Prescott, and J. Svarc (2001), Inversion of GPS data for spatially variable slip-rate on the San Andreas Fault near Parkfield, CA, *Geophys. Res. Lett.*, *28*(2), 359–362.

Nadeau, R., and L. Johnson (1998), Seismological studies at Parkfield VI: Moment release rates and estimates of source parameters for small repeating earthquakes, *B. Seismol. Soc. Am.*, *88*(3), 790–814.

Nadeau, R., and T. McEvilly (1997), Seimological studies at Parkfield V: Characteristic microearthquake sequences as fault-zone drilling targets, *B. Seismol. Soc. Am.*, *87*(6), 1463–1472.

Nadeau, R., and T. McEvilly (1999), Fault slip rates at depth from recurrence intervals of repeating microearthquakes, *Science*, *285* (5428), 718–721.

Nadeau, R., W. Foxall, and T. McEvilly (1995), Clustering and periodic recurrence of microearthquakes on the San Andreas Fault at Parkfield, California, *Science*, *267*(5197), 503–507.

Ogata, Y. (1988), Statistical models for earthquake occurrences and residual analysis for point processes, *J. Am. Stat. Assoc.*, 9–27, San Francisco, Calif.

Pacheco, P. (1997), *Parallel Programming with MPI*, Morgan Kaufmann.

Peng, Z., and Y. Ben-Zion (2005), Spatiotemporal variations of crustal anisotropy from similar events in aftershocks of the 1999 M7. 4 Izmit and M7. 1 Düzce, Turkey, earthquake sequences, *Geophys. J. Int.*, *160*(3), 1027–1043.

Peng, Z., and P. Zhao (2009), Migration of early aftershocks following the 2004 Parkfield earthquake, *Nat. Geosci.*, *2*(12), 877–881.

Perfettini, H., and J. Ampuero (2008), Dynamics of a velocity strengthening fault region: Implications for slow earthquakes and postseismic slip, *J. Geophys. Res.*, *113*, B09,411.

Perfettini, H., and J. Avouac (2004), Postseismic relaxation driven by brittle creep: A possible mechanism to reconcile geodetic measurements and the decay rate of aftershocks, application to the Chi-chi earthquake, Taiwan, *J. Geophys. Res*, *109*(10.1029), B02304.

Perfettini, H., J. Avouac, and J. Ruegg (2005), Geodetic displacements and aftershocks following the 2001 m_w= 8.4 Peru earthquake: Implications for the mechanics of the earthquake cycle along subduction zones, *J. Geophys. Res. B*, *110*(B9), B09,404.

Perfettini, H., et al. (2007), Modeling afterslip and aftershocks following the 1992 Landers earthquake, *J. Geophys. Res.*, *112*(B7), B07,409.

Press, W. H., S. A. Teukolsky, W. T. Vetterling, and B. P. Flannery (2007), *Numerical Recipes Source Code CD-ROM 3rd Edition: The Art of Scientific Computing*, 3 ed., Cambridge University Press, New York.

Rice, J. (1992), Fault stress states, pore pressure distributions, and the weakness of the San Andreas Fault, *Int. Geophys. Ser.*, *51*, 475–475.

Rice, J. R. (1993), Spatio-temporal complexity of slip on a fault, *J. Geophys. Res.*, *98*, 9885–9907.

Rice, J. R., and A. L. Ruina (1983), Stability of steady frictional slipping, *J. Apll. Mech.*, *50*, 343–349.

Rubin, A., and J. Ampuero (2005), Earthquake nucleation on (aging) rate and state faults, *J. Geophys. Res.*, *110*, B11,312.

Ruina, A. L. (1983), Slip instability and state variable friction laws, *J. Geophys. Res.*, *88*, 10,359–10,370.

Schaff, D., G. Beroza, and B. Shaw (1998), Postseismic response of repeating aftershocks, *Geophys. Res. Lett.*, *25*(24), 4549–4552.

Segall, P., and J. Rice (2006), Does shear heating of pore fluid contribute to earthquake nucleation? *J. Geophys. Res.*, *111*, B09,316.

Skarbek, R., A. Rempel, and D. Schmidt (2012), Geologic heterogeneity can produce aseismic slip transients, *Geophys. Res. Lett.*, *39*(21), L21306, doi:10.1029/2012GL053762.

Sorensen, D. (1992), Implicit application of polynomial filters in AK-step Arnoldi method, *SIAM J. Matrix Anal. A.*, *13*(1), 357–385.

Swarztrauber, P. (1982), *Vectorizing the Fast Fourier Transforms, in Parallel Computations*, Garry Rodrigue, Academic Press, New York.

Swarztrauber, P. (1984), FFT algorithms for vector computers, *Parallel Comput.*, *1*(1), 45–63.

Titus, S., C. DeMets, and B. Tikoff (2006), Thirty-five-year creep rates for the creeping segment of the San Andreas Fault and the effects of the 2004 Parkfield earthquake: Constraints from alignment arrays, continuous global positioning system, and creepmeters, *B. Seismol. Soc. Am.*, *96*(4B), S250–S268.

Tse, S., and J. Rice (1986), Crustal earthquake instability in relation to the depth variation of frictional slip properties, *J. Geophys. Res.*, *91*(B9), 9452–9472.

Utsu, T. (1972), Aftershocks and earthquake statistics (3): Analyses of the distribution of earthquakes in magnitude, time and space with special consideration to clustering characteristics of earthquake occurrence (1), *J. Fac. Sci., Hokkaido U. Ser. 7, Geophys.*, *3*(5), 379–441.

Utsu, T., Y. Ogata, and R. Matsu'ura (1995), The centenary of the Omori formula for a decay law of aftershock activity, *J. Phys. Earth*, *43* (1), 1–33.

Zheng, G., and J. Rice (1998), Conditions under which velocity-weakening friction allows a self-healing versus a cracklike mode of rupture, *B. Seismol. Soc. Am.*, *88*(6), 1466–1483.

Ziv, A., and A. Cochard (2006), Quasi-dynamic modeling of seismicity on a fault with depth-variable rate-and state-dependent friction, *J. Geophys. Res.*, *111*, B08,310.

Ziv, A., and A. Rubin (2003), Implications of rate-and-state friction for properties of aftershock sequence: Quasi-static inherently discrete simulations, *J. Geophys. Res.*, *108*(2051), 21.

Ziv, A., A. Rubin, and D. Kilb (2003), Spatiotemporal analyses of earthquake productivity and size distribution: Observations and simulations, *B. Seismol. Soc. Am.*, *93*(5), 2069–2081.